Broadening the Thin-Film horizon

Opto-electrical modelling of a monolithic Perovskite/CIGS tandem solar cell

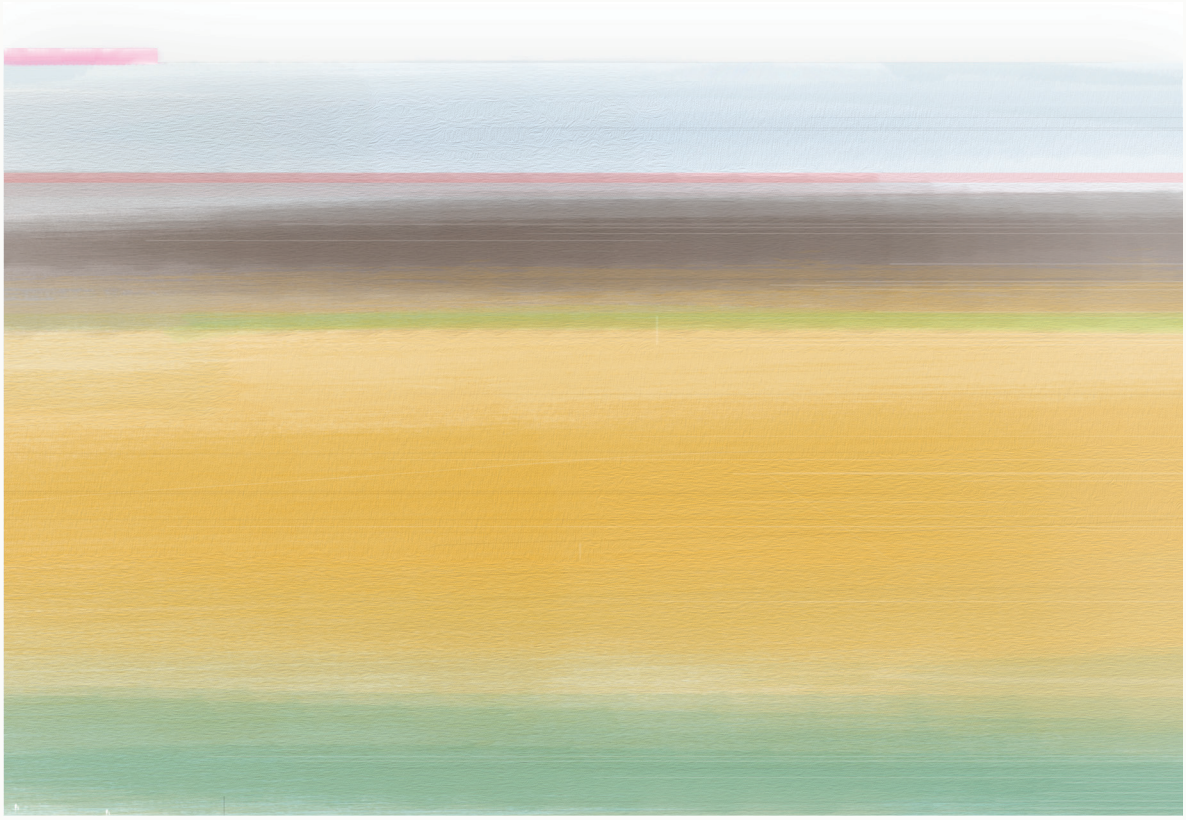

Jelle Knobbe
TU Delft

Broadening the Thin-Film Horizon

Opto-electrical modelling of a monolithic Perovskite/CIGS tandem solar cell

by

Jelle Knobbe

in partial fulfillment of the requirements for the degree of

Master of Science
in Sustainable Energy Technology

at the Delft University of Technology,
to be defended publicly on December the 6th, 2021 at 14:00

Student number:	4363787		
Project duration:	March 2021 – December 2021		
Thesis Committee:	Dr. Paul Procel Moya	TU Delft, PVMD - EWI	Daily Supervisor
	Dr. Nasim Rezaei	University of Twente	Daily Supervisor
	Prof. Dr. O. Isabella	TU Delft, PVMD - EWI	Internal Committee Member
	Dr. S.W.H. Eijt	TU Delft, TNW	External Committee Member

TU Delft Delft University of Technology

Abstract

The need for more efficient, cheaper, easily producible solar cells is growing as this combination of attributes can decrease the levelized cost of energy (LCOE). A two-terminal (2T) Perovskite and gallium-inidium-gallium-selenide (Pvk/CIGS) tandem cell is an excellent candidate, as it can have a power conversion efficiency (PCE) of +30%, can be flexible (making it suitable for roll-to-roll production), and the deposition of a Pvk solar cell (PSC) on top of established techniques like CIGS will only add one extra step to the production process, thereby improving the PCE significantly

This thesis is part of LAFLEX-2T project which aims to design and engineer a highly efficient flexible 2T thin-film solar device based on the Pvk/CIGS tandem configuration. The aim of this thesis is to develop an opto-electrical model of the tandem configuration which replicates the inner physics of a reference solar cell. This can be used to give insights on the current losses occurring in the cell and on the limitations in the charge carrier transport towards the electrodes. Based on this analysis, a route of improvements is proposed with could result in more efficient solar cells.

The simulation template uses optical and electrical simulations based on GENPRO4 and TCAD Sentaurus, respectively. An extensive model for Pvk/CIGS tandem cells is presented and validated using experimentally obtained J-V curve measurements. It was found that charge transport in the tunnel recombination junction (TRJ) depends on direct energy and in-direct energy transfer, in terms of two tunneling mechanisms: band to band tunneling (B2BT) and trap assisted tunneling (TAT). For TAT, a non-local model facilitated by trap states is successfully implemented.

Simulation results reveal that the transport in the TRJ of the reference solar cell is based on TAT. The loss analysis points out that reflectance losses are responsible for a loss of 10.92 mA/cm^2. Similarly, losses due to parasitic absorption are equal to 5.32 mA/cm^2. The CIGS bottom was identified as the current limiting layer. The dominant recombination mechanisms in the Pvk and CIGS absorber layer are Shockley-Read-Hall (SRH) and surface recombination calculated as 4.71 mA/cm^2 and 1.59 mA/cm^2 for top Pvk and bottom CIGS, respectively. An increase in losses in the absorber layers in maximum power point (MPP) compared to short circuit (SC) conditions exposed charge transport issues in the collecting path of charge carriers.

After assessing the loss mechanisms, a road-map for efficiency improvements is proposed. After implementation, an increase in the PCE of the reference tandem cell was observed from 10.63% to 26.69%.

Acknowledgments

Although a thesis is mostly done alone, in the last nine months it never felt like it was. It has been a hectic period with many restrictions in our normal way of doing. But by adaptation to the situation still, a lot of opportunities arose. Completing the final hurdle in the path to receiving the master's degree in Sustainable Energy Technology has been an important accomplishment in my life.

This accomplishment could not have been reached without the help of a specific group of people. First, I want to thank Prof. Dr. Olindo Isabella for not only providing me with this research subject but also actively helping me with the search for a topic that would fit my interests.

Nasim Rezaei, for being the supervisor other people can only wish for. I looked forward to our almost daily exchanges, which covered topics from electron transport to family, from lines of code to the Tomb of Hafez. Not once after starting, have I regretted my choice to switch from my first to this subject. Thank you for giving me the opportunity to work together on this topic.

Paul Procel, for your willingness to teach me everything I asked for and your unlimited knowledge on the not-so user-friendly programs that we have used. You gave me the tools to thrive in the last months after you took over from Nasim. Both you and Nasim have shown me that research is a team effort and new things are built on top of the old.

Daan, for working alongside each other towards the end of our master degrees. It has helped me a lot. Thank you for reminding me about what the important things in life are.

Pap and mam, for being there when needed, motivating me and providing me with a place where I could fully focus on the project without any distraction, until the end and always.

My friends at home, for giving me the much-needed distraction from this thesis in the form of cooking, drinks, and talks. And specifically Victor Wijn for designing the front cover.

Jelle Knobbe
Rotterdam, December 2021

Contents

Nomenclature

Abbreviations

ALD	Atomic layer deposition
B2BT	Band to band tunneling
Br	Bromine
CB	Conduction band
DOS	Density of states
DT	Direct tunneling
ETL	Electron transport layer
F	Fluorine
FA	Formamidinium
FCA	Free-carrier absorption
FF	Fill factor
Ga	Gallium
HTL	Hole transport layer
In	Indium
IR	Infrared
ITO	Indium tin oxide
IW	Illumination window
MA	Methylammonium
Mo	Molybdenum
NiO	Nickel Oxide
NIR	Near infrared
O	Oxygen
PCBM	Phenyl-C61-butyric acid methyl ester
PCE	Power conversion efficiency
PTAA	poly(triaryl)amine
PV	Photovoltaic
SnO_2	Tin Oxide
TAT	Trap assisted tunneling
TCAD	Technology Computer-Aided Design

TCO	Transparent conducting oxide
TE	Thermionic emission
TRJ	Tunneling recombination junction
VB	Valence band

Constants

$\hbar$	Reduced Planck constant
A^*	Effective Richardson constant
k_b	Boltzmann constant
q	Elementary charge

Symbols

α	Absorption coefficient
β	constant of proportionality
χ	Electron affinity
ΔE	Misalignment CB and VB in TRJ
ΔE_n	Energy difference conduction band and Fermi level
ΔE_p	Energy difference Fermi level and Valence band
ϵ_0	Absolute dielectric permittivity
ϵ_x	Dielectric function
Γ	Tunneling probability
μ	Mobility
ϕ_x	Workfunction of compound *x*
ψ	Electrostatic potential
ρ	Electric charge
σ	Capture cross section
τ	Carrier lifetime
ε	Energy level
C_c^n	Electron capture rate
D	Diffusion coefficient
E	Electric field
e_c^n	Electron emission rate
E_F	Fermi energy
$E_{g,x}$	Bandgap energy of compound *x*
E_{VB}	Valence band energy
f_t	Electron occupation of defects

g	Degeneracy factor
I_0	Incident light intensity
IE	Ionization energy
J_x	Current density
J_{SC}	Short circuit current
k	Extinction coefficient
m_e^*	Effective electron mass
m_n^*	Effective electron mass
N	Complex refractive index
n	Refractive index
N_e	Free carrier density
R	Recombination rate
s_x	Surface recombination velocity
V_{OC}	Open circuit voltage
V_r	Build-in voltage
v_{th}	Thermal velocity

List of Figures

List of Tables

1
Introduction

Long has the world looked for a way to create energy out of nothing [7]. With the discovery of the photovoltaic effect, this dream has come awfully close to becoming a reality. With techniques that can utilize the sun as an energy provider, the looming threat of a rapid increase in energy consumption per capita and the rise in the number of people walking on this earth, ensuing in growth in total energy needed, can be covered by a more long-term sustainable energy solution [8]. To further increase the impact of solar energy, it is of great importance that challenges regarding the conversion from sunlight to electricity in an efficient and cost-effective way will be tackled.

In this thesis the optical and electrical properties of a promising solar cell, containing a combination of metal halide perovskites and copper indium gallium selenide (CIGS), will be modelled and studied, thereby creating a guide for the eventual experimental fabrication of the cell.

In section 1.1, the potential and history of solar cells will be highlighted. General information on tandem cells and an introduction to the absorber layer materials is done in section 1.2. Section 1.3 gives an overview of previous work done on perovskite/CIGS solar cells and explains the configuration of the baseline tandem cell used in this thesis. The reason for simulating solar cells and an overview of the modelling approach is mentioned in section 1.4. To conclude, the outline, objective, and structure of the project are summarised (section 1.5).

1.1. The potential and a brief history of solar cells

As mentioned in the section above, solar power can play a significant role in the transition from fossil fuels towards a society run primarily on renewable energies, including wind, biomass, geothermal, etc. According to the International Renewable Energy Agency, 50% of the total energy consumption by 2050 will be provided by electricity. 90% of this will be sourced from renewable energy sources which equal about 160 EJ [9]. As of 2020, around 600 GW of solar power capacity is installed worldwide, but will continuously grow for the coming years. In 2050, solar PV and wind will lead the way; the installed PV capacity will reach over 14,000 GW, compared to wind with over 8,100 GW [9]. The rapid increase in installed PV power can be contributed to the rapid developments in this sector, leading to competitive levelized costs of electricity (LCOE) compared to that of fossil fuels [10].

When considering these numbers, it is even more remarkable that the first practical solar cell was only publicly demonstrated a few decades ago, with an efficiency measured of 6% [11]. The working principle of a solar cell was first observed by Becquerel in 1839 at the age of 19, by fabricating an electrolytic cell, made out of two platinum electrodes, placed in an electrolyte (an electrically conducting solution) [12]. After an earlier breakthrough with a junction based on platinum and selenium, the first properly working solar cell with an efficiency of 1% was developed in 1883 by Charles Fritz based on a gold-selenium junction.

The real development of solar cells as we know it, started with the silicon-based solar cell made at the *Bell Laboratory* in the United States by Daryl Chapin, Calvin Fuller, and Gerald Pearson in 1954 [11]. From then on, multiple academic institutes and industries started to develop silicon-based solar cell with the main focus in space application, propelling the progress leading to the dominance of silicon-based solar cells we see today [12]. The foundation for the subject of this thesis was seen in 1980 when the first thin-film solar cells based on a copper-sulfide/cadmium-sulfide junction were demonstrated with a conversion efficiency above 10% at the *University of Delaware*. Later in time, a dye-sensitized solar cell (DSSC) with high efficiency was published by the *École polytechnique fédérale de Lausanne* in Switzerland by Michael Grätzel in 1991 [12] opening up the new research field which would eventually lead to the development of the perovskite solar cell in 2009 [13].

Although the PV market is primarily dominated by silicon-based wafers (about 95%) [12], some

materials have the potential to become the next big thing. Two of those, which are the focus of this thesis, are solar cells based on the previously mentioned perovskites and CIGS, which if combined in a tandem architecture, potentially could outperform standard single-junction silicon cells [2].

1.2. The perovskite/CIGS tandem

Tandem cells are interesting for thin-film technologies, as they can overcome the practical efficiency limitations of a single-junction solar cell which is 33.16% [14]. This could potentially increase to 45% in tandem. In the total cost of a solar panel, on average, the module only accounts for 18% [15]. Most cost is related to the balance of system (BOS) which includes wiring, inverters and the mounting. A module with a high efficiency will therefore directly affect the LCOE as the BOS for installed power will significantly reduce.

Next to potential high efficiency for the perovskite/CIGS solar cell, there are more reasons to dive into this subject. Research has shown that perovskite can relatively easily and cost-effectively be deposited on top of already existing and well-performing technologies like CIGS and silicon single-junction solar cells via low-temperature solution methods [16] adding just some extra steps in the production process. Also, monolithic perovskite/CIGS tandem cells will be compatible with lightweight flexible plastic or metal foil for roll-to-roll manufacturing, which will reduce production cost even further.

This section will give some more insights on tandem cells in general, as well as the two used absorber layers.

Tandem cell configurations

To enhance the *power conversion efficiency* (PCE) and make better use of the solar spectrum, two absorber materials with different bandgap energies can be combined in one stack, also known as a tandem cell [17]. By covering the light spectrum in two parts, and optimizing the layers for their assigned wavelengths, the PCE can be increased. The top layer is the absorber with the highest bandgap, absorbing the high-energy photons (which is equal to light with a short wavelength). The bottom cell will therefore absorb the lower energy photons (larger wavelength) and consequently has the smaller bandgap [12]. Furthermore, the material in the top needs to be transparent for the photons of low energy to allow them to pass to the lower absorber [18]. This can reduce the so-called thermalization loss of the charge carrier which is the excess photon energy lost as heat.

An important aspect of a tandem cell is the current matching. The lowest generated current density in the top or bottom layer will determine the total current density of the complete stack. This will limit the possible higher current density that could be reached and this will therefore directly affect the efficiency of the cell. If the current densities can be matched, a better distribution of the generated current could be reached. It could increase the eventual current density of the cell together with the *conversion efficiency* [12]. A tandem can be seen as two solar cells connected in series. According to Kirchhoff's law, the tandem voltage is the sum of the voltages generated by the two subcells.

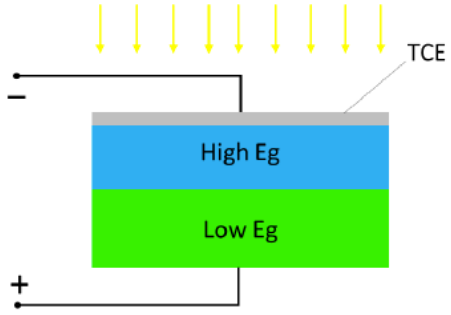

(a) Two-terminal monolithic stack where the absorber layers are deposited on top of each other, resulting in the need for current matching [1].

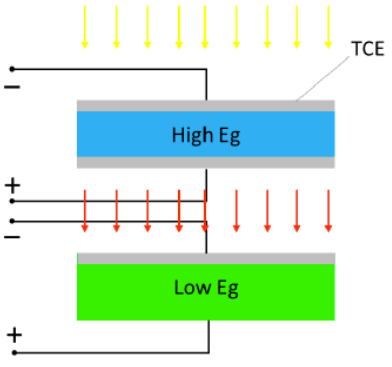

(b) Four terminal architecture with two separate subcells. Although less sensitive to spectral variation, extra layers and cabling are needed [19].

Figure 1.1

Based on the number of terminal connections, tandem cells are divided into three types: two-terminal (2T), three-terminal (3T), and four-terminal (4T) tandem solar cells [1]. 2T and 4T are the most common in literature for perovskite/CIGS solar cells. When two cells are independently wired, it is called a 4T architecture. As the cells do not have to be current-matched, they will be less sensitive with respect to spectral variations, but it requires extra transparent conducting layers (TCO) and additional cabling and powerpoint tracker [2]. Figures 1.1a and 1.1b show the difference in the most common configurations and visualize the need for extra layers in 4T cells.

By design, the 4T architecture will need to separate cells with an assembly somewhere along the production line. Meaning, it could be considered as two separate devices which, without being connected and just placed side by side, could perform better and deliver more power than stacked. The 2T architecture however is one monolithic unit, produced as one inter-connected cell in series, where every layer is deposited on top of the other [2]. Also, theoretically, the 2T configuration has the same performance as the 4T when the cell is at the optimum bandgap [1].

The Tandem Region

The engineering and production of a 2T tandem cell bring a lot of challenges to the table. Not only do the cells need to be current-matched, but the bottom cell must be engineered to be a substrate for the top-cell deposition. The eventual power output is dependant on bandgaps, quantum effiencies, the V_{oc} loss that can occur at both cells and the spectral transmission of the top cell. An estimate of the maximum efficiency for perovskite/CIGS solar cells as a function of two bandgaps is seen in figure 1.2. After an analysis done by Jacobsson et al. [2] it was concluded that PCE of 30+% is attainable, considering the state-of-the-art technologies for individual perovskite and CIGS cells, and all the layers in the device stack are optimized.

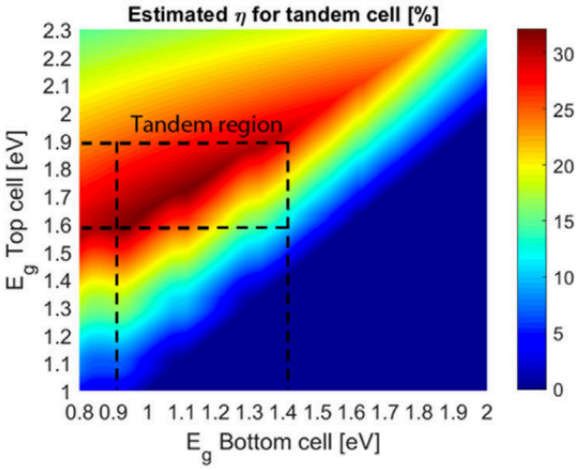

Figure 1.2: Estimate of maximum device performance of a perovskite/CIGS tandem cell as a function of the two bandgaps, taking in to account the state-of-the-art for both technologies [2]

The figure clearly shows that the feature of having a tunable bandgap for both cells is beneficial for reaching top efficiencies. According to equations 1.1 and 1.2, there is a perovskite composition for every possible CIGS bandgap. Making it thereby possible to adjust the materials to one another so a current-matching tandem cell is achieved. More information on the two absorber layers can be found in the subsection 1.2.

$$E_{g,CIGS} = 1.68x + 1.03(1-x) - 0.12x(1-x)$$
$$x = Ga/(Ga+In) \tag{1.1}$$

$$E_{g,perovskite}(x,y) = 1.58 + 0.436x - 0.0580y + 0.294x^2 + 0.0199xy$$
$$x = \frac{[Br]}{[Br]+[I]}, y = \frac{[FA]}{[FA]+[MA]} \tag{1.2}$$

CIGS

CIGS can be classified as part of the chemical family called chalcopyrites. These materials are composed of elements from groups I, III, VI found in the *periodic table*. Together, they form a tetragonal crystalline structure, in which each group-I and III atom bonds with four group-VI atoms in a tetrahedral format, and each group-VI atom bonds with two group-I and two group-III atoms [20]. By changing the composition of CIGS, the bandgap of the material can be tuned. The equation for the composition is given by equation 1.1, in which x takes values between 0 and 1. CIS and CGS can have bandgaps between 1 and 1.71 eV, respectively [21]. CIGS is considered to be a direct bandgap material.

As the project is performed in close collaboration with TNO and the eventual cell will be fabricated by them, their standard configuration of CIGS solar cells will be used. It consists of a glass substrate, molybdenum (Mo) back contact, CIGS absorber and CdS buffer layer which will be briefly talked about.

The most common substrate used is soda-lime glass (SLG). It is favorable for its high thermal stability, similar thermal expansion coefficient as CIGS, and the sodium (Na) content that can diffuse into the CIGS [22].

The most popular back contact for CIGS cells is Mo because of its stability during high-temperature growth of the CIGS layer when fabricating the cell. It also forms an ohmic contact with CIGS [21]. Because of its low resistance, the charge flows easily both ways. However, due to the high absorption coefficient and the low reflectivity, the material is unfavourable for the optical performance. These aspects result in absorption of light without reflecting it back into the solar cell which has a negative influence on the efficiency. On top of the Mo layer, the CIGS is deposited, which is followed by the so-called buffer layer. In a normal CIGS cell, the buffer layer would be positioned between the absorber and the TCO layer. But in the tandem cell, the buffer is situated between CIGS and the recombination layer which will be described in section 1.3. The buffer layer (n-type) is used to form the p-n junction and has multiple roles. It gives a better lattice match between the absorber and the transparent mid-layer (mid TCO). It also protects the CIGS surface during the sputtering of the mid transparent layer and creates a buried junction to prevent losses via recombination of minority carriers [12].

The layer consists of a few nanometers of CdS. As Cd is a toxic material and CdS has high parasitic absorption, the research world has sparked interest in other relevant materials that could be used such as $Zn(O,S)$, Ln_2S_3, $(Zn,Mg)O$ and $(Zn,Sn)O$ [22].

Perovskite

Perovskites are organic-inorganic hybrid materials with the general chemical equation of ABX_3. '*A*' is the monovalent organic cation like methylammonium (MA, $CH_3NH_3^+$) and formamidinium (FA,$CH(NH_2)_2^+$), which is also often mixed [2]. The B is the metal cation, such as lead-ion Pb(II) and tin-ion Sn(II), where *B* is smaller than *A*. The *X* is the halide (i.e. Cl^-, Br^-, I^-). The 3 components form the general cubic crystal structure of perovskite [23]. The best performing perovskites today have a composition comparable to $\mathrm{Cs_{0.05}FA_{0.79}MA_{0.16}PbBr_{0.49}I_{2.51}}$ [24]. The bandgap of this material is around 1.7 eV which makes it suitable as a top cell layer in the tandem configuration. The bandgap can be increased by increasing the ratio of Br. Although, in access of 40-50% a phase instability where phase separation is observed into I and Br richer regions, which decrease the cell performance [25]. Not only the tunable bandgap is reason for the interest in the material. There are other desirable properties of perovskite like high carrier mobilities, high absorption coefficient and long charge carrier diffusion length. The perovskite solar cell (PSC) exists in two types of solar cells, thin-film solar cells and multi-junction solar cells.

An important phenomenon to mention is the so-called hysteresis. Depending on the voltage scan direction (forward or reverse) and scan rate, the J-V curve can have significant differences. This can cause over- or underestimations of the device performance. Hysteresis is a well-documented phenomenon but the underlying processes are not well understood and multiple suggestions about the origin are made. Some examples are trapping or de-trapping of charge carriers, ion-mitigation or ferroelectric behaviour of the perovskite [26, 27]. Some research has shown that defects near the electron transport layer and perovskite (ETL/perovskite) interface potentially cause the anoumalous hysteresis [28]. The hysteresis effect will not be researched in this thesis as it is out of the scope of this thesis.

Previous work on perovskite/CIGS tandems

The combination of a perovskite/CIGS solar cell was first proposed in Yang et al. in 2015 [29] and has been topic of research from then on [30–32]. When cells consist of two different absorber mate-

rials, there can be multiple ways of engineering the eventual architecture of the cell [30]. Table 1.1 summarizes the work that has been done on the perovskite/CIGS solar cells for both the 2T and 4T configuration. For the 4T, the cell characteristics can be measured for each absorber layer, so only the total cell efficiency is mentioned. For this thesis, only a monolithic 2T perovskite/CIGS solar cell is considered.

Source	Type	J_{sc} (mA/cm^2)	V_{oc} (V)	FF %	PCE (η) %
		2-terminal			
[18]	Modelling	20.49	1.81	81.8	30.5
[33]	Modelling	15.79	1.69	72.9	27.6
[32]	Experimental	18.0	1.58	76.0	21.6
[34]	Experimental	16.10	1.45	68.2	15.9
[2]	Experimental	13.5	1.57	70.0	15.0
[31]	Experimental	17.3	1.77	73.1	22.4
		4-terminal			
[35]	Experimental	-	-	-	28.0
[36]	Experimental	-	-	-	25.9
[15]	Experimental	-	-	-	22.1
[37]	Experimental	-	-	-	23.4
[38]	Experimental	-	-	-	20.7
[39]	Experimental	-	-	-	17.8

Table 1.1: Characteristics overview of published work on perovskite/CIGS solar cells, both modelled and experimental. As hysteresis causes different forward and reverse values, the average is taken.

1.3. The baseline tandem stack

This thesis project is based on a very specific configuration of a perovskite/CIGS solar cell, which was developed in collaboration with TU Eindhoven, TU Delft, TNO, UHasselt, within LAFLEX-2T project consortium. The LAFLEX-2T project has the goal to deliver a higly efficient monolithic 2T flexible perovskite/CIGS tandem cell with a PCE of above 19%. This section will give more insight into the work done on perovskite/CIGS solar cells and give a layer-by-layer configuration of the baseline tandem. Next to the standard configuration of the subcells discussed in earlier sections, more layers in the tandem cell are needed to create a fully energy-aligned stack. For the needed extra layers, the function and possible materials are briefly mentioned including the one used for the baseline tandem configuration in this thesis.

Figure 1.3 shows the configuration of the perovskite/CIGS solar cell. The cell can be divided in three main parts, the perovskite top layer, the CIGS bottom layer, and the connecting tunneling recombination junction (TRJ). The perovskite top layer consists of the absorber material, perovskite, a hole transport layer (HTL), and an electron transport layer (ETL), which make sure generated charge carriers are separated and move in opposite direction towards either an electrode (the electrons) or the towards the TRJ (the holes), which consist of the PEDOT:PSS and sALD SnO_2 layer. This junction makes sure that non-collectible generated carriers in both absorber layers can recombine. Non-collectible charge carriers are the charge carriers that are not collected at one of the electrodes. The CIGS bottom layer consists of the earlier mentioned CIGS absorber layer, CdS HTL and the needed mid TCO. In the following subsections, the remaining layers are discussed in more depth.

The mid TCO

On the top of the buffer layer of CIGS a transparent conductive oxide (TCO) is deposited. This layer needs to be conducting, transparent, and must fit the energy alignment. The TCO layer is only required to conduct in a vertical manner as it only transports charge carriers towards the top or bottom, no lateral conduction is needed. Decreasing the parasitic absorption in the NIR/IR-region (Near infrared/infrared) of light is important as these are the wavelengths that reach the bottom cell. Two materials that have properties that meet the requirements are aluminium doped zinc oxide (AZO), intrinsic ZnO (i-ZnO),

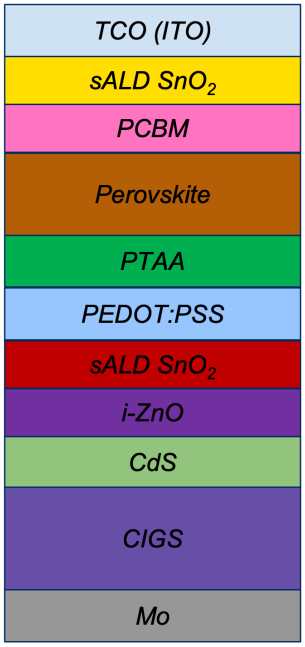

Figure 1.3: The monolithic Perovskite/CIGS tandem cell stack configuration used in this thesis, including an inverse Psc on top of a standard CdS/CIGS stack connected via the TRJ.

and intrinsic SnO_2 (ITO) [2]. The used mid TCO in the thesis baseline tandem is i-ZnO in combination with SnO_2.

The HTL

Due to the polarity of the CIGS, the configuration of perovskite needs to be in the "inverted" configuration (p-i-n) [32]. This means an HTL layer must be deposited first on top of the mid-TCO layer. This recombination layer between the cells needs to be transparent, energetically aligned with nearby layers and act as hole-selective contact with respect to the perovskite, and act as a good substrate for deposition of the perovskite material.

Typical HTL for this configuration are poly(triaryl)amine (PTAA) , PEDOT:PSS or a metal oxide such as Nickel Oxide (NiO_x) and Tin Oxide (SnO_2) [32]. Jost et al. (2019) suggest a double HTL composed of NiO_x and PTAA would be beneficial for perovskite tandem cells which increased the V_{oc} due to reduction of recombination at the HTL/perovskite interface which is referred to as a bilayer. In literature, more combinations of the HTL materials used for bilayers are suggested like PEDOT:PSS/PTAA [40]. This combination does not need the use of any metal oxides, which is beneficial as their chemistry is complicated with a lot of variety in their stoichiometry [41], have different phases [42] and a number of different possible surface oxides [43]. The baseline tandem cell has a PTAA/PEDOT:PSS as the HTL, in which PEDOT:PSS also plays a role in the tunnel recombination junction.

The ETL

For the functioning of a perovskite tandem cell, there is a need for an ETL layer which needs to have the right energy alignment, electron selective for charge carriers, and be transparent for IR to UV. For the p-i-n configuration fullerene Phenyl-C61-butyric acid methyl ester (PCBM) is most used. Another material that is often seen is C60 which is chemically very similar to PCBM. Also, SnO_2 can be used but brings similar problems as was seen for other metal oxides for HTL [2].

The optimization of the ETL layer is an ongoing topic. The possibility of adding a high bandgap insulator like LiF or MgF2 in the ETL is mentioned in literature [44]. LiF and MgF2 are often used as an anti-reflective coating but could possibly passivate shunts and reduce surface recombination [2]. For the baseline tandem material combination of PCBM and SnO_2 is used.

Tunneling Recombination Junction

To achieve a monolithic solar cell, a tunneling recombination junction (TRJ) is sandwiched between the top and bottom cell and connects the cells in series. This interface between the two absorber layers,

should next to electronically couple these layers, also ensure efficient charge recombination of minority carriers, sans inducing majority carrier recombination in the top or bottom layer. Recombination of majority carriers would reduce the collected current and equal current losses. Recombination in the TRJ is facilitated by the possibilities of charge carriers tunneling through empty states according to quantum mechanics [45]. According to the current matching principle, explained in section 1.2, an even amount of electrons and holes should be collected at each subcell's contact interface thereby creating the current matching conditions. The properties of its TRJ are an additional factor that strongly determines the overall tandem performance. It can simultaneously affect its J_{SC}, FF and V_{OC}.

In tandems, the two layers that make up the TRJ for perovskite/CIGS are mostly the ETL and HTL of the respective subcells. Thereby it could be said that the carrier transport layers fulfill two roles; 1. collecting charge carriers and 2. enabling efficient minority-carrier recombination [46]. As mentioned above, the mid SnO_2 layer together with the PEDOT:PSS layer will function as the TRJ.

1.4. Modelling of tandem cells

The previous section showed the layer configuration and the role of the different layers in the perovskite/CIGS tandem cell. As synthesizing and testing different materials with different properties can be very time-consuming, modelling of the cell containing realistic semiconductor physics and material properties could be a solution. As more layers are added to the configuration of a solar cell, the complexity of understanding the eventual effect of certain materials cannot be described analytically or be explained by simple reasoning. Luckily, numerical simulation can be used to simulate underlying physics within semiconductors to compare and analyze proposed devices. By modelling, the effect of certain changes to a configuration can be predicted, resulting in guidelines for the eventual fabrication of the cell in the lab. This could speed up research significantly.

Opto-electronic modelling of tandem cells has previously been reported [47–49]. The models mostly reduce the cell to a one-dimensional (1D) model, neglecting the electron and hole fluxes into y- and z-direction and mostly consider single trap level and density distribution for perovskite layers [18]. Secondly, the TRJ is often modelled as a direct energy aligned junction, mainly based on band to band tunneling without considering all the possible tunneling mechanisms that can occur [50].

This thesis presents a unique two-dimensional (2D) model, using a combination of accurate and fast optical generation profile modelling by using the GenPro4 software [51] and the fundamental semi-conductor physics modelling with the TCAD Sentaurus software. By not only solving the standard partial differential equations, but also including detailed recombination models induced by defect states in material bulk and interfaces, and accurate tunneling mechanisms in the top and bottom connecting TRJ based on direct (B2BT) and indirect (TAT) tunneling mechanisms, the inner physics of a tandem solar cell can accurately be reproduced. This can lead to a deep understanding of the of the losses in the cell. This information can then be used for targeted optimization approaches. Not only will this be useful for perovskite/CIGS tandem cells, but for all different tandem material combinations, or even multi-junction devices.

1.5. Project description and outline

The aim of this thesis is to study the physical mechanisms ruling the performance of thin film perovskite/CIGS tandem solar cells by using optical and electrical modelling approaches. An example tandem cell configuration developed within the LAFLEX-2T project, figure 1.3, was used as baseline for the model. From this study, the optical and electrical bottlenecks regarding the current losses in the cell can be identified and optimizations are suggested regarding light management techniques, material choices, and parameters. This can then be used as a guideline for the experimental optimization of the same stack, which can result in speeding up the progress of reaching a high-efficiency perovskite/CIGS flexible thin-film tandem cell.

The objectives of this thesis can be divided in three main points:

1. Develop a realistic modelling template for the perovskite/CIGS baseline tandem cell
2. Perform an optical and electrical loss analysis of the baseline tandem cell
3. Propose recommendations and guidelines for the optimization of the baseline tandem cell

Chapter 2 will give an introduction to the theoretical background. In chapter 3, the simulation approach and additions to the tandem model are explained, including tunneling mechanisms in the tunnel recombination junction. After validation of the proposed tandem model, the electrical and optical bottlenecks are extracted and presented in chapter 4, including an analysis of the carrier transport in the TRJ. Finally, in chapter 5, the optical and electrical optimization guidelines are presented which could result in a high efficiency perovskite/CIGS tandem solar cell.

2
Theoretical Background

The following chapter will provide background information regarding the fundamental workings of a solar cell and give more insights in understanding the modelling principles, explained in chapter 3. In section 2.1 the basic semiconductor physics concepts will be explained. Section 2.2 will give an overview of the most important recombination mechanisms. Lastly, section 2.3 will give more information on the transport in heterojunctions and the different tunneling mechanisms.

2.1. Fundamental physics for a solar cell

Simulation models of semiconductor devices like solar cells do not have the computational capacity to calculate the movement of every particle in a device. However, it can use semi-classical models to describe the physics of solar cells. The movement of charge carriers can be described using Newton's laws, and the properties of particles are determined by the quantum theory of solids. Some concepts are briefly described. For a detailed explanation of semiconductor physics, we refer to Neamen [3].

2.1.1. p-n junction

To understand the behaviour of charge carriers in semiconductor devices, the theory behind doping should be explained. At the absolute zero point (0 K), no electrons from the valence band will be situated in the conduction band. At temperatures above this point, *thermal excitation* will take place when sufficient thermal energy is provided by the interaction of electrons with the vibration of the lattice of atoms and molecules in the semiconductor material. The electrochemical potential of electrons in materials is described by the Fermi level (E_F), which indicates the average electron energy. It can be used as a measure to determine the occupancy of energy states. For intrinsic materials, the Fermi level is positioned around the middle of the bandgap. If the effective mass of electrons and holes are not exactly equal, the effective density of states (DOS) will not be symmetrical and a shift for the Fermi level away from the middle will occur [3].

The concentration of either holes or electrons in semiconductor materials can be altered via doping. When doping a material, the intrinsic atoms are replaced by so-called dopants which exhibit a different concentration of electrons in the valence band than the intrinsic material thereby altering the Fermi level position. The process of swapping intrinsic atoms with the dopant impurities is called doping. If the added impurities have more valence band electrons, the material becomes n-type, and the Fermi level moves closer to the conduction band. When intrinsic material is substituted with materials with less electrons in the valence band, the material becomes p-type and the Fermi level energy moves closer to the valence band.

These n-type and p-type material can form a p-n junction which facilitates the charge carrier transport and separation needed to have a functioning solar cell. When considering one type of material (with similar ΔE_g) the junctions is called homojunction. For different materials (which is most common in a tandem solar cell consisting of 13 layers) a heterojunction is formed, subsection 2.3 will give more information on this topic. The difference in free charge carrier concentration near the junction results in diffusion. Electrons will diffuse from the n-type region to the p-type region and vice versa for holes. The depletion of the majority charge carriers results in the formation of an electric field, acting as a second driving force in the opposite direction of diffusion. The junction becomes almost depleted from free charge carriers, a so-called *depletion region* is formed. Figure 2.1 gives an overview of the different mechanisms and regions in a p-n junction in equilibrium.

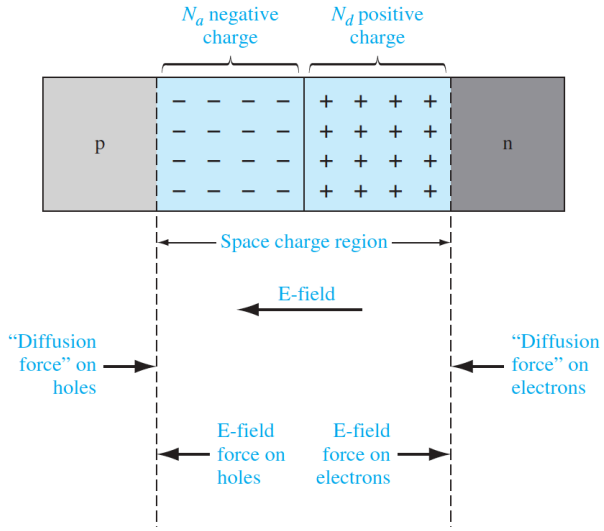

Figure 2.1: The space charge region, the electric field, and the forces acting on the charge carriers for an example p-n junction [3]

2.1.2. Poisson equations

The Poisson equation relates volume density of electric charges ρ to the build-in potential $V(r)$. The charge density is dependant on mobile and immobile charges. The mobile charge carriers are electrons (n) and holes (p). The stationary charges originate from the doping concentration of the materials. Materials and regions can be doped with donor (n-type) or acceptor (p-type) atoms. N_D and N_A are the concentration of these ionised donor and acceptor atoms. The contribution of possible trap states within the solar cell to the density of charges is indicated with ρ_{trap}, see equation 2.1. The elemental electrical charge ($q = 1.602 * 10^{-19}C$) is the charge contribution of every dopant and carrier.

$$\rho = q * \left(p - n + N_D^+ - N_A^-\right) - \rho_{trap} \tag{2.1}$$

The charge density is related via the permittivity ϵ_r of the materials to the electric field E and can be used, according to the *Poisson equation* 2.2 to calculate the electrostatic potential ψ. For simplicity, the one-dimensional formula is given. The vacuum permittivity ϵ_0 is value of the absolute dielectric permittivity in vacuum and equals $8.8565 * 10^{-12}F/m$.

$$\frac{d^2\psi(x)}{dx^2} = -\frac{dE(x)}{dx} = \frac{-\rho(x)}{\epsilon_r\epsilon_0} \tag{2.2}$$

Solving the *Poisson equation* results in the eventual profile and shape of electrostatic potential, which is the band diagram of the proposed solar stack, including the width of the depletion region and the build-in voltage V_{bi}.

2.1.3. Drift and Diffusion

Two main transport mechanisms are considered, drift and diffusion, which are part of the so-called drift-diffusion model. Drift is the movement of carriers caused by an electric field and diffusion is caused by a gradient in carrier density. Charge carrier transport in semiconductors follow the continuity equation, as charge conservation needs to be maintained. Equation 2.3 is used for electrons, and equation 2.4 for holes.

$$\nabla J_n = qR_{net,n} + q\frac{\partial n}{\partial t} \tag{2.3}$$

$$-\nabla J_p = qR_{net,p} + q\frac{\partial p}{\partial t} \tag{2.4}$$

The R_{net} is the net recombination rate. The charge carrier transport (driven by drift and diffusion) determines the current density observed in the semiconductor.

A concentration gradient can cause a driving force for charge carriers to move through a semiconductor device. This current is driven by the size of the gradient and the diffusion coefficient (D). This gives two equations, both related to the electrons and holes, respectively:

$$J_{diff,n} = qD_n \nabla n \tag{2.5}$$

$$J_{diff,p} = -qD_p \nabla p \tag{2.6}$$

If an electric field is present, it can cause the movement of charge carriers, accelerating them in the direction dependant on the charge of the carrier and the direction of the field. Holes move with the electric field, and electrons do the opposite. The mobility (μ) relates the movement of the carriers to the electric field via equations 2.7 and 2.8, and is material dependant.

$$J_{drift,n} = -q \cdot n \cdot \mu_n \cdot E \tag{2.7}$$

$$J_{drift,p} = q \cdot p \cdot \mu_p \cdot E \tag{2.8}$$

2.2. Generation and Recombination

As mentioned in the previous chapter, various recombination mechanisms are present in a solar cell. This can be both beneficial and unfavourable for the working of the solar cell. In the following section the most important mechanisms will be explained, including general generation of charge carriers and radiative, Auger and Shockley-Read-Hall recombination. If a solar cell is in equilibrium, and no illumination is taking place, the generation rate is equal to the recombination rates. During illumination, an excess of charge carriers is generated, resulting in two options. The first is the collection of a charge carrier at an electrode and secondly, the recombination of the carrier, as no accumulation of carriers in the device is possible (continuity equation). There are multiple ways of recombination, which will be briefly explained below.

Direct recombination

This direct recombination mechanism or band-to-band recombination is the process of charge carriers directly recombining and releasing energy in the form of radiation (photon emission). This mechanisms is most relevant for the direct bandgap materials like the main absorber materials used in this thesis (perovskite and CIGS). The recombination rate is directly proportional to the number of available empty states where β in equation 2.9 is the constant of proportionality which are often in the order of 10^6 for direct bandgap materials, and $n_{i,eff}$ is the intrinsic carrier density [3].

$$R_{net} = \beta \left(np - n_{i,eff}^2 \right) \tag{2.9}$$

Auger recombination

Auger recombination is a three-particle process and is most predominant in indirect bandgap materials. The process is based on the conservation of energy and momentum of the holes and electrons when recombining. During recombination, part of the momentum and energy is transferred to a third carrier (either an electron or holes), exciting the charge carrier deeper into the valence band (for a hole) or deeper into the conduction band (for a electron). The third excited charge carrier will eventually relax to the edge of the band edge and transfer its energy as a phonon into the lattice of the atom or molecule [12]. As this mechanism is mostly dominant in indirect bandgap materials, it is of less relevance for the perovskite/CIGS model.

Shockley Read Hall recombination

Due to the misalignment of atoms in the material structure, defects can occur. These defects exist within the bulk or around the interface of a junction, mostly in the form of impurity atoms and lattice defects. These defects can allow energy states within the forbidden bandgap, which can potentially act as steppingstones for transfer mechanisms or as recombination centers, and are often referred to as traps. The energy level at which the recombination centers are situated is referred to as E_T. A probability exists that the traps capture both electrons and holes, which is mostly related to the

capture cross-section. One can assume that the probability of capturing the different charge carriers is approximately equal [3]. This process of recombination via trap states within the bandgap is referred to as Shockley Read Hall (SRH) or indirect recombination.

Two types of traps can be considered; donor- and acceptor-type. The donor type is neutral and the acceptor is negatively charged when filled with an electron. Charge carriers can be captured and emitted, resulting in four processes that can contribute to SRH recombination. This is trap occupation dynamics and can be seen in figure 2.2. Four processes can be considered:

1. Capture of an electron from the conduction band
2. Emission of an electron to the conduction band
3. Capture of an electron from the valence band
4. Emission of an electron to the valence band

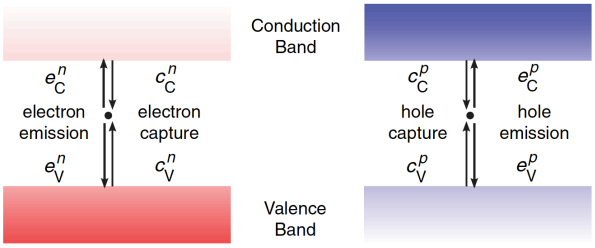

Figure 2.2: Trap occupation dynamics, on the left electron and on the right hole capture and emission dynamics [4].

The occupation of traps by an electron can be expressed by equation 2.10, where C_C^n is the electron capture-rate from the conduction band of an empty defect, and e_C^n is the electron emission rate to the conduction band of an occupied defect. The V denotation refers to the valence band. The electron occupation of defect (f_t) can be represented by a value between 0 or 1 (empty or full, respectively).

$$\frac{\partial f_\mathrm{t}}{\partial t} = (1 - f_\mathrm{t})\, c_\mathrm{C}^n - f_\mathrm{t} e_\mathrm{C}^n + (1 - f_\mathrm{t})\, c_\mathrm{V}^n - f_\mathrm{t} e_\mathrm{V}^n \tag{2.10}$$

The capture rate can be expressed as a product of the thermal velocity (v_{th}), the capture cross section (σ) and the charge carrier density at the defect, resulting in the following equations for electron capture:

$$c_\mathrm{C}^n = \sigma_n v_\mathrm{th}^n n \tag{2.11}$$

When all processes are combined, an equation for the recombination rate can be found. Recombination occurs when both an electron and hole are attracted in the same trap. Equation 2.12 gives the recombination rate, where the σ_n and σ_p are the capture cross-sections for electrons and holes, N_T the defect density, g is the degeneracy factor, and V_{th} the thermal velocity. The E_F and E_T are the Fermi energy and trap energy, respectively.

$$R_{net} = \frac{N_0 v_{th}^n v_{th}^p \sigma_n \sigma_p \left(np - n_{i,eff}^2\right)}{v_{th}^n \sigma_n \left(n + n_1/g_n\right) + v_{th}^p \sigma_p \left(p + p_1/g_p\right)} \tag{2.12}$$

with:

$$\begin{aligned} n_1 &= n_{\mathrm{i,eff}} \exp\left(\frac{E_\mathrm{T}}{k_b T}\right) \\ p_1 &= n_{\mathrm{i,eff}} \exp\left(\frac{-E_\mathrm{T}}{k_b T}\right) \end{aligned} \tag{2.13}$$

When no traps are modelled in the material, SRH is estimated by using the carrier lifetime τ.

Surface recombination

Surface recombination occurs due to dangling bonds at the different material interfaces and can be viewed as defects. These dangling bonds cause trap states and recombination centers to be formed. Via the earlier explained SRH recombination, this mechanism contributes to the current losses in solar cells.

Although very similar, the recombination rate is mainly dependant on the surface recombination velocity. This parameter is dependant on the doping concentration at the surface [4]. This results in an additional formula:

$$R_{\text{surf, net}}^{\text{SRH}} = \frac{np - n_{\text{i,eff}}^2}{(n + n_1)/s_p + (p + p_1)/s_n} \tag{2.14}$$

where s_n and s_p are the surface recombination velocity.

2.3. Transport in heterojunctions

Within layer stack configurations with different materials, heterojunctions exist. The heterojunction refers to a situation where the two materials that make up the junction have different bandgaps and/or electron affinities (χ). This results in an offset between the conduction and valence bands often denoted as ΔE_C and ΔE_V. These discontinuities at the edges can result in the formation of barriers that could negatively affect the transport of charge carriers in the solar cell. The transport in heterojunctions is based on diffusion, thermionic emission (TE) [3] and different tunneling mechanisms [3, 52] which will be discussed more thoroughly as it is of great importance in the workings of the TRJ.

The current related to the thermionic emission is a function of the concentrations of electrons which have sufficient x-directed velocity. For electrons, the distribution with respect to energy in the conduction band results in a fraction of the electrons having the needed energy to overcome the barrier (E_B) in heterojunctions. The thermionic emission current can be expressed in a model by equation 2.15 where the ϕ_{Bn} is the barrier height. Often the left part of the equations is referred to as the reverse saturation current (J_{st}).

$$J = \left[A^* T^2 \exp\left(\frac{-q\phi_{Bn}}{k_b T}\right)\right]\left[\exp\left(\frac{qV_a}{k_b T}\right) - 1\right] \tag{2.15}$$

The *effective Richardson constant for thermionic emission* (A^*) is given by the following equation where m_n^* is the effective electron mass:

$$A^* \equiv \frac{4\pi q m_n^* k_b^2}{h^3} \tag{2.16}$$

For a more thorough and comprehensive derivation of the constant one can look at Neamen [3].

Tunneling

Tunneling is the phenomenon were a charge carrier's total kinetic energy is lower than the necessary energy to overcome a barrier, but can still penetrate and appear on the other side of the barrier. Quantum mechanics explains that there is a finite probability of tunneling happening. Within semiconductors, three different mechanisms are found: direct tunneling (DT), band to band tunneling (B2BT) and *trap assisted tunneling* (TAT).

Direct tunneling refers to the principle of charge carriers tunneling through a barrier but remaining in the same energy band (e.g. conduction band to conduction band). The transport of holes from the valence band in a p-typed region to a conduction band in an n-type region or vice versa for electrons and holes is based on the B2BT or the TAT. The B2BT mechanism is only possible when the mentioned bands are properly energetic aligned. The condition, activation energy (E_a) of the p-type region needs to be smaller than the energy gap between the Fermi energy and conduction band of the n-type region, which needs to be satisfied. TAT occurs both with a energetic aligned and misaligned bands as traps facilitate energy states within the bandgap, increasing the tunneling probability. Vijayan et al. [53] suggest DT and B2BT mechanisms being dominant for energetic band-aligned junctions, but argue that the TAT mechanism dominates the transport when the band alignment gets worse.

Finding the probability of tunneling through a barrier requires solving the Schrödinger's equation for the electron wave function [54]. To simplify the equation, this is mostly done in the perpendicular direction of the interface and with the approximation of the effective charge carrier mass. If the potential of the barrier changes slowly with position (meaning the change in potential on each electron wavelength should be small compared to the energy of the particle), an approximate solution to the Schrödinger's position can be found. This is called the Wentzel-Kramers-Brillouin approximation (WKB) and is the basis of calculation of the tunneling current in the model. The full derivation can be found in Merzbacher et al. [55].

To model the tunneling in a TRJ through a barrier, the tunneling current is converted into a local generation or recombination process, $G_{Tun}(r)$, which is mostly dependant on the Fermi level, work-function and potential profile along the tunneling path [56]. The local J_{Tun} is related to the G_{Tun} via equation 2.17, where ψ, ε and E are the electrostatic potential, the energy level and the electric field.

$$G_{\text{Tun}}(r) = \frac{1}{q}\nabla \cdot J_{Tun} = \frac{1}{q}\frac{dJ_{Tun}}{d\psi} \cdot \nabla\psi = \frac{dJ_{Tun}}{d\varepsilon} \cdot E \tag{2.17}$$

The local tunneling generation rate is described as:

$$G_{Tun}(r) = \frac{A^*T}{k_B}\vec{E} * \Gamma(r) * \ln\left[\frac{1+\exp\left(-q\left(\psi-\phi_n\right)/k_BT\right)}{1+\exp\left(-q\left(\psi-\phi_m\right)/k_BT\right)}\right] \tag{2.18}$$

where Γ is the tunneling probability, and k_b the Boltzmann constant. The other parameters are already mentioned earlier in this chapter. The equations indicates that the tunneling generation is directly proportional to the probability.

The WKB approximation for the tunneling probability:

$$\Gamma(r) = \exp\left[-\frac{2}{\hbar}\int_0^r \sqrt{2m\left(\phi_b/q + \phi_m - \psi(x)\right)}dx\right] \tag{2.19}$$

where $\hbar$ is the Planck constant, m is the tunneling mass. It can be seen from the equation that the tunneling probability will decrease with increased energy barriers. Different ways to overcome this barrier are the B2BT and the TAT mechanism.

Trap assisted tunneling

As mentioned before, next to B2BT, TAT exists. In this process, subgap energy states (like defects or dangling bonds) can act as two things. First as a charge trapper and secondly for charge transfer, within the recombination mechanism referred to as the capture and emission processes. This dynamics of processes is mostly determined by the defect energy distribution closely situated to the Fermi level as the probability of capture and emission of charge carriers is on par. Thus the energy of the subgap states determines if a state contributes to the charge or discharge. When closely situated to the Fermi level, the probability of capturing or emission of a charge carrier is around 50% making the trap suitable to contribute to the TAT mechanism [57].

The most important parameters for the TAT process are the following [52]:

- Trap density
- Trap distribution
- Trap occupancy dynamics
- Tunneling Energy barrier

When thinking about subgap states, it should be considered that these energy states play a role in two mechanisms, SRH recombination (see subsection 2.2) and the TAT.

The TAT can be divided in to two different mechanisms: inelastic and elastic TAT. When the needed energy to reach a subgap state is paired with the emission of a phonon (the oscillation of the lattice of an atom or molecule [3]) the mechanism is referred to as inelastic. The phonon is emitted after relaxation of the charge carrier in to the trap state and eventually will be converted in to thermal energy [58]. The elastic TAT however does not see any change of energy level for the charge carriers and is

mostly considered to be the dominant mechanism for direct bandgap materials [59]. For this model, the inelastic TAT and thus phonon emission is not considered.

TCAD Sentaurus is able to calculate the net recombination rate of the non-local tunneling model and the full derivation can be found in the manual [4].

3
Simulation approach and Calibration

Before an optical and electrical loss analysis of the baseline Perovskite/CIGS tandem cell can be done, a comprehensive model of the solar device first needs to be developed that will replicate the inner physics of the cell. The methodology for doing so is presented in this chapter. First the general modelling approach is explained (section 3.1) containing an optical part (section 3.2) and electrical part seen in section 3.3. After detailing the included physics models in the electrical model, the approach of modelling the TRJ is explained in section 3.4. The last section details the calibration approach of the model 3.5.

3.1. General simulation approach

To research the monolithic tandem Perovskite/CIGS semiconductor device, a general modelling approach was used. The *GENPRO4* [60] software is utilised to obtain the optical generation profile for a proposed layer stack. This was used as input for the Sentaurus TCAD to perform the electrical simulations.

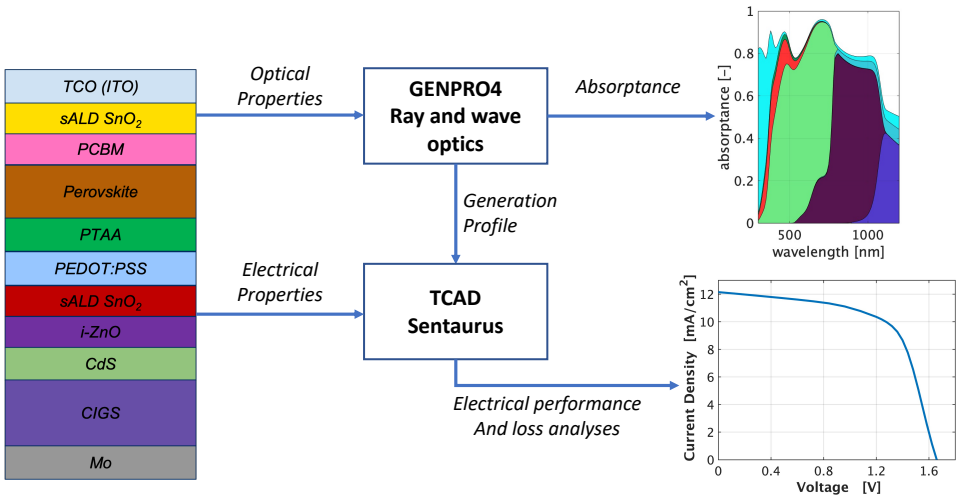

Figure 3.1: The general modeling approach makes use of the optical profile generated by the *GENPRO4* software [51]. This optical generation profile is used in combination with the electrical model built in TCAD Sentaurus to obtain the electrical performance.

As the complexity of the Sentaurus model increases with every different layer, the amount of possible variable combinations and their effect on the electrical properties and performance becomes harder to study. When dealing with a structure of eleven layers of different materials and electrical properties, the fitting of the cell parameters with experimental values is too complex. Therefore, it was decided to split the tandem cell into two single-junctions models (Perovskite and CIGS). After validation with experimental J-V curve data obtained from in-house measurements [61], the two models could be combined, keeping the electrical parameters constant. After combining the two models, the tandem model was validated by calibrating the electrical parameters in the layers that form the connection

between the top and bottom cells: the tunnel recombination junction (TRJ). In flowchart 3.2 the overall process is summarized.

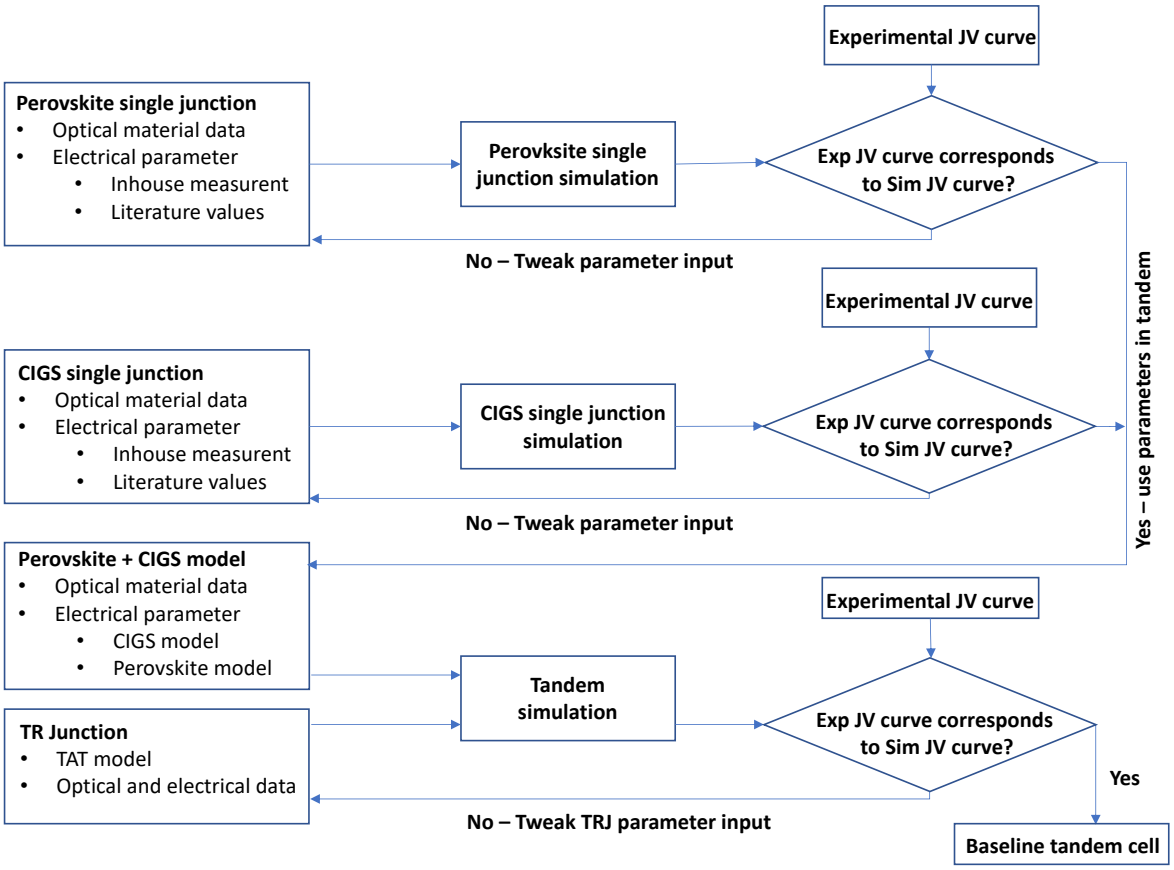

Figure 3.2: A flowchart that describes the overall thesis approach to reach the eventual baseline tandem cell used for opto-electrical analysis.

As the methodology described in this thesis contains three different models (Perovskite, CIGS, and tandem model), the concepts of optical and electrical modeling are explained in a more general sense as well as the cell geometry and doping. The model-dependant additions like spatial trap distribution (Perovskite) and bandgap grading (CIGS) are explained for specific materials. General additions like heterojunction transport including thermionic emission and tunneling, which is observed in both models are described from the general modelling perspective.

To properly explain the general approach of the project, one should first understand the tools being used as well as the modelling approach for the most important aspects of the tandem device.

3.2. Optical modelling

As mentioned, for the optical generation profile within the solar cell devices the software *GENPRO4* was used which was developed at the TU Delft. The software combines wave and ray-optics by taking into account the light scattering and potential light trapping at the interfaces of materials. By knowing the wavelength dependant refractive index of each medium denoted by n_x, the light trapping and scattering can be calculated. The software does also takes the Beer-lambert law into account [62] which indicates that with penetration depth in a material, the incident light intensity I_0 attenuates exponentially when travelling through absorbing medium. The equation 3.1, also known as Beer-Lambert's equation, is depth dependant (z). The absorption coefficient α is material and wavelength dependant and can be calculated using the extinction coefficient k.

$$I(z) = I_0 exp(-\alpha z) \tag{3.1}$$

$$N = n + ik \tag{3.2}$$

For every material, the complex refractive index (N) and thickness are needed as input. For this solar cell, the interfaces were assumed to be flat, meaning the conventional net-radiation method [62] was used to calculate reflectance, transmittance, and absorptance (R, T, A respectively). Figure 3.3 is an example of a used complex refractive index for the front ITO layer in the baseline tandem configuration.

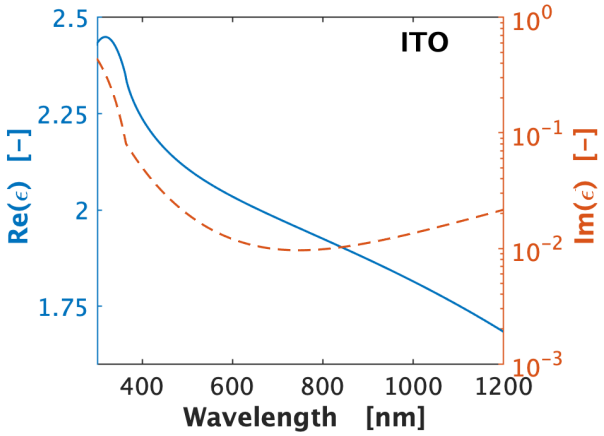

Figure 3.3: An example of the wavelength-dependent n and k values for the front ITO in the model that are used as input for the *GENPRO4* software with the real part (Re) being n and imaginary part (Im) being k.

The total incident photocurrent density J_{ph} is the summation of all calculated current densities in every layer, including the R an T over the wavelengths 300 nm to 1200 nm. *GENPRO4* uses a stepsize of about 10 nm and an incident photon flux from AM1.5 light spectrum. The integration of the tandem cell adds up to a density of 46.45 mA/cm^2. The generation profile throughout the depth of the cell structure for all different layers is the input for the electrical model.

3.3. Electrical modelling

For this study, the *Synopsys Sentaurus* (version 2015.6) was used for the electrical simulation model. This program contains multiple tools that can be used to simulate the inner physics of semiconductor devices. A two-dimensional simulation approach was used for this thesis. The model is built in different steps which will be explained in the following subsections. First, the device structure needs to be generated which is done using Sentaurus Structure Editor (SDE) as will be explained in section 3.3.1.

The actual device simulation is performed in Sentaurus Device (SDEVICE). Within SDEVICE, optical, thermal, and electrical simulations can be executed. This thesis focuses on the electrical model capabilities as the temperature is kept constant and the optical data is provided by *GENPRO4*. To solve the semiconductor equations described in chapter 2, including recombination and generation models, thermionic emission, and tunneling at interfaces and junctions, an initial guess is made. This is called Newton's method. Because of the high complexity of the model, often, it does not converge and does not result in a solution. Therefore the mesh refinement, step size of the solve steps, or device parameters need to be adjusted manually. Sentaurus Visual (SVISUAL) is used to analyse the results ensuing from simulations. A detailed analysis can be made of the proposed device structure, including energy band diagram, different recombination currents, trap induced recombination, tunneling currents, and carrier densities.

3.3.1. Solar cell geometry and doping

The geometrical model, built in SDE, is based on the features obtained from the reference solar cells, including width and contact area. The modelling was done in a 2-D simulation to save computational time as research has shown no significant difference can be observed when comparing results to a 3-D model [63]. The width of the simulation is based on the symmetry plane found in the tandem reference cell and is set to an eighth of the actual width (about 500 μm). The reference tandem cell

contains contact fingers in a u-shape. As only the symmetry plane is used, the resulting contact is only found in the top left corner. As the width of the fingers is equal to 280 nm on a total cell width of 4.0 mm, the ratio contact/width is 0.07 resulting in a contact width of 35 μm for the 500 μm wide cell.

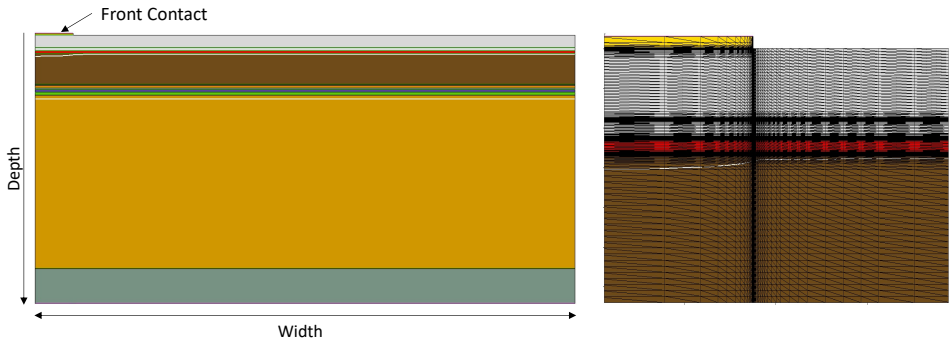

Figure 3.4: On the left the geometrical features of the 2-D solar tandem cell is seen, including the width and depth. The front contact is placed in the left top corner. On the right, a close up of the mesh is shown, including the refinements when moving towards interfaces.

To simplify the model, all interfaces are considered flat. All doping profiles in the materials were considered uniform and can be found in section 3.5. The mathematical models inside the device are solved using numerical discretization schemes, meaning the model needs a subdivision with geometrical shapes on top of the generated structure to solve the equations. These geometric shapes are referred to as a mesh. In the simulation, the mesh becomes more refined and smaller near the interfaces to accurately calculate charge transport (as the gradients of carrier density become larger) and the possible interface recombination. The meshing is of great importance for the convergence of the solar cell model. Materials that were considered to be of more importance (like the absorber layers) and needed more detailed modelling, had finer defined meshes in the bulk. As all interfaces could be viewed as heterojunctions, where possible recombination or tunneling mechanisms could occur, a very fine mesh was defined. For tunneling mechanisms in the TRJ, non-local meshes were needed. This will be explained in more depth in subsection 3.3.5.

3.3.2. Included physics models

As the purpose of the model will be to analyse the optical and electrical bottlenecks of the perovskite/CIGS tandem cell, it is needed to include the most important physics models described in chapter 2 to make the model replicate the inner physics of the experimentally obtained solar cell. Table 3.1 summarizes the used models.

Table 3.1: Summary of most relevant physical models and parameter used in the electrical model

Model parameters	Implemented model
Semiconductor	
Free carrier statistics	Fermi-Dirac
Mobility	Canali [64]
Intrinsic recombination: radiative	Parameters perovksite in [28]
	Parameters CIGS in [22]
Thermionic emission	
Intrinsic carrier denisty	No bandgap narrowing
SRH recombination	Scharfetter [65]
Cross section model	Poole-Frenkel
Interfaces	
Surface SRH	Scharfetter [65]
Band to band Tunneling	Non-local tunneling model [4]
TAT tunneling	Ieong [56]

3.3.3. Bandgap grading CIGS

In the CIGS material the bandgap can be engineered by varying the GGI according to the energy shift model [22]. The GGI was modelled with the following approach: a linear decrease from the CdS/CIGS interface with a GGI value of 0.32 towards the so-called tipping point (TP) at 500 nm with a GGI of 0.22, from this TP the GGI increases linearly to 0.4 at the bottom interface [66]. The liner profile is a simplified approach to the bandgap grading effect on the performance of the CIGS single-junction.

$$GGI = [GA]/([GA] + [Ln]) \tag{3.3}$$

A deeper insight in the overall CIGS model can be found in Rezaei [22].

3.3.4. Modelling of defects

In chapter 2 the role of trap states in the working of a solar cell were explained. The goal in this thesis was not to model the exact complicated nature of defects in the both absorber layers, but rather mimic the performance of the single-junction solar cells regarding potential recombination processes and to potentially research the enhancing effect of passivating the interface situated defects [66]. Also, the implemented trap distribution was used to calibrate the single-junctions with the experimental obtained J-V curve by altering the defect concentration [67]. In the simulation for the CIGS single-junction, the defects in the CIGS bottom layer is modelled as donor-type mid-gap energy states that function as recombination centres . A second acceptor-like defect distribution was added in the CIGS layer at 0.2 eV from the VB [66].

Table 3.2: A presentation of the different implemented trap densities in the single and tandem models. The spatial concentration in perovskite refers to the modelling of trap density increase when moving from the bulk to both interfaces. For the interface traps of CIGS/CdS interface, a level energy distribution is used.

Traps							
Layer parameters	Symbol [unit]	CIGS	CIGS	CdS	CIGS/CdS	i-ZnO	Perovskite
Concentration	N_T $[cm^{-3}]$	$5{*}10^{13}$	$1{*}10^{12}$	$5{*}10^{15}$	$1{*}10^{12}$	$1{*}10^{16}$	spatial
Type	-	D	A	A	A	A	D
Energy level	E_T	E_i	0.2 eV(VB)	E_i	E_i	E_i	E_i
Standard deviation	E_S $[eV]$	0.5	0.5	0.5	0.5	0.5	-
Cap. cross-sec	σ_e $[cm^2]$	$5{*}10^{-13}$	$5{*}10^{-13}$	$5{*}10^{-13}$	$1{*}10^{-15}$	$1{*}10^{-15}$	$1{*}10^{-17}$
	σ_h $[cm^2]$	$1{*}10^{-15}$	$1{*}10^{-15}$	$1{*}10^{-15}$	$5{*}10^{-13}$	$5{*}10^{-13}$	$1{*}10^{-17}$

For the modelling of the mid-gap states in perovskite, also described as deep-level states, the profile found in Ni et. al [5] was used for the spatial distribution. This paper describes a clear increase in trap state density when moving towards the interfaces. Two types of defects are considered in the model: acceptor- and donor-like defects which are described in section 2.2. For the modelling of deep-level defects in perovskite an exponential equation is used, resembling the documented density profile in Psc thin films [5]:

$$N_{\mathrm{T}} = N_{\mathrm{T,\,bulk}} + N_{\mathrm{T,ETL}} \exp\left(\frac{x_{\mathrm{ETL}} - x}{\delta_{\mathrm{ETL}}}\right) + N_{\mathrm{T,HTL}} \exp\left(\frac{x - x_{\mathrm{HTL}}}{\delta_{\mathrm{HTL}}}\right) \tag{3.4}$$

Table 3.3: Trap state concentrations for the bulk and interfaces

Region	Symbol	Concentration
Perovskite/PTAA	$N_{T,HTL}$	$1{*}10^{17}$ cm^{-3}
Perovskite/PCBM	$N_{T,ETL}$	$1{*}10^{15}$ cm^{-3} [68]
Perovskite Bulk	$N_{T,Bulk}$	$1{*}10^{14}$ cm^{-3}

The values for the trap state concentration parameters are given in table 3.3. The δ gives a value to the depth of defect density at the interfaces which is equal to 0.1 μm. The X_{ETL} and X_{HTL} are the depth of the interfaces in μm. The modelled result is seen in figure 3.5.

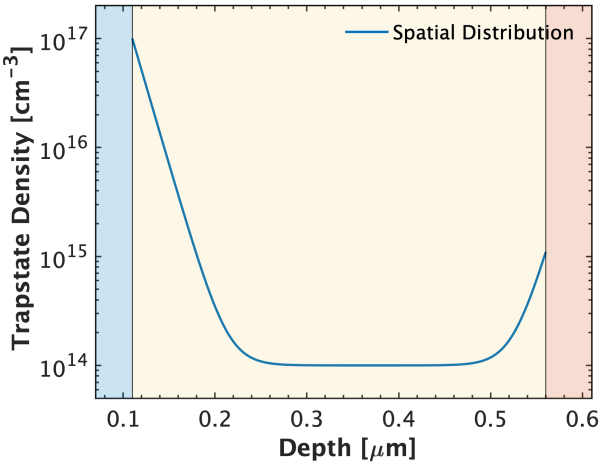

Figure 3.5: The spatial distribution of trap states in the perovskite layer adapted from [28] and based on the work of Ni et al. [5]. Blue area represents the PTAA layer while the red area represents PCBM. The trap density increases when approaching both interfaces compared to the bulk value.

For the energetic distribution of traps in the model, a Gaussian distribution is used. In equation 3.5 the N_T represents the maximum trap state density given in table 3.2. The E_T is the maximum energy level op traps, and E_s is the standard deviation.

$$N_{T,E} = N_T \exp\left(-\frac{(E - E_T)^2}{2E_S^2}\right) \tag{3.5}$$

3.3.5. Heterojunction transport modelling

As the model contains multiple combinations of materials with different bandgaps and electron affinities (see section 3.5), various heterojunctions are formed. Conventional transport equations can not be applied thus the need for different transport mechanisms arises [4]. The following transport mechanisms in heterojunctions are implemented: *thermionic emission* and *tunneling* [4]. As the selection for tunneling models is quite extensive for Sentaurus, the non-local tunneling model is chosen as it takes into account the complicated band edge profile, which directly relates to the tunneling current and its less needed computationally power [4]. The method is described in section 2.3.

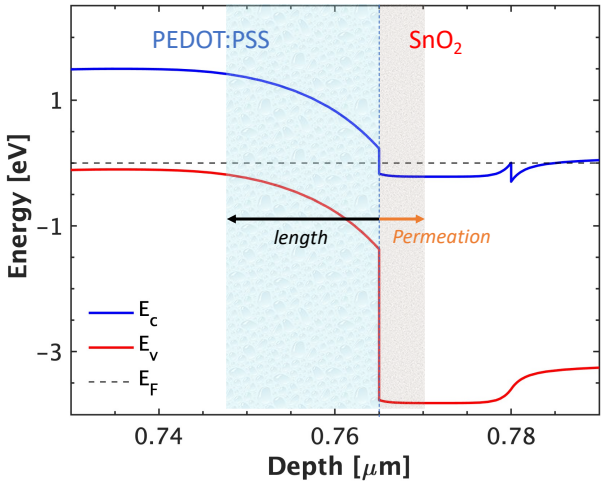

Figure 3.6: An example of a non-local mesh modelled at a heterojunction interface including the length and permeation.

The tunneling current depends on the band edge profile that is situated between two coupled points that are connected via tunneling. As the shape is often complex, by solving the transport and Poisson equations, SDEVICE is able to compute the current. As this does not happen locally, but for the entire

band edge profile, the tunneling process is considered to be non-local.

The connected two points on either side of the interface are defined by a *non-local mesh* which are non-local lines that indicate the possible tunneling path for holes and electrons. In the model, it is necessary to specify this *non-local mesh* for every interface or junction (which will be explained in more detail in the next section) where potential tunneling could take place. In the tandem model this was done at all interfaces to increase the accuracy of the obtained results. The non-local mesh is defined at an interface and consists of two parts, a *length*, which is the tunneling path in to the bulk of one of materials at the interface. The second part is the *permeation*, which is the distance the tunneling path penetrates in to the other material. An example is given for the PEDOT:PSS/SnO_2 junction in figure 3.6.

3.4. The tunnel recombination junction

In chapter 2 the need for TAT and the concept behind it was explained. This chapter explained the choice for the non-local tunneling model that can be used for direct tunneling and B2BT. Although a bit more complex to model, the TAT can be modelled as a non-local process too. This results in an mechanism where the possible tunneling current is not only dependant on the energy level change of the charge carrier but also on the barriers that need to be overcome when carriers hop in to intraband situated trap states [4], see figure 3.7a and figure 3.7b for a comparison of the mechanisms.

As the junction can be seen as an abrupt heterojunction, most models that require TAT, make use of local variables. This makes them not suitable for the modelling of the TRJ [69, 70]. The non-local TAT model uses the WKB method (see section 2.3) to exactly calculate the energy barrier along the profile, thus resulting in an accurate computation of the TAT in the TRJ. In the Dynamic non-local path TAT, charge carriers are captured by or emitted from defect states.

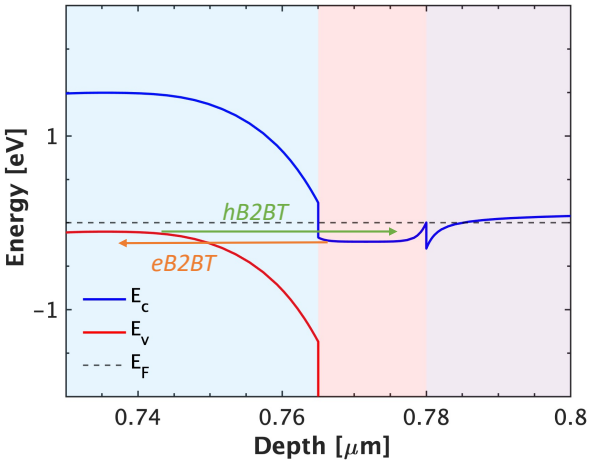

(a) A visualization of the eB2BT and hB2BT mechanisms. This process is possible with proper band alignment of the VB of PEDOT:PSS (blue area) and the CB of SnO_2 (red area) across the equivalent energy states.

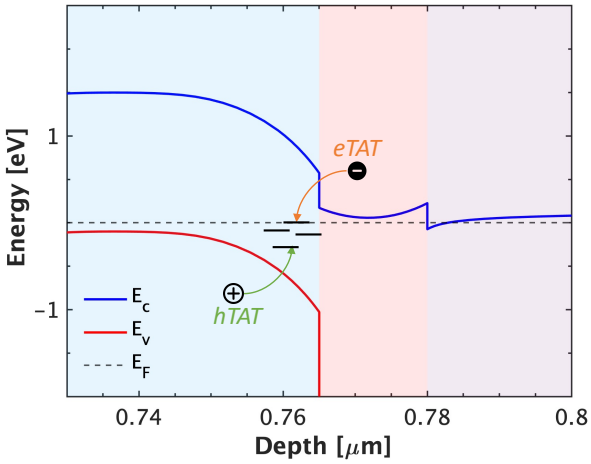

(b) A visualization of the eTAT and hTAT mechanism where subgap energy states (traps) act as carrier reservoirs for charge transfer or charge trapping.

Figure 3.7

Traps can be coupled to nearby situated interfaces via the non-local meshes, providing a tunneling path to and from the trap states. To model TAT through a barrier, two separate non-local meshes need to be created, providing a tunneling path for each side of the traps. In the tandem model the subgap energy states will be situated in the PEDOT:PSS layer, resulting in non-local meshes at the PTAA/PEDOT and PEDOT/SnO_2 interfaces, see figure 3.8. The penetration depth of non-local mesh positioned at the PEDOT/SnO_2 interface was set to the thickness of the PEDOT:PSS material, thereby making sure that the tunneling mechanism could happen for different band alignments. As different voltage biases are applied during the J-V curve sweep in the model, different alignments and band bending of the VB and CB in the TRJ occur. By choosing an overestimation of the proposed tunneling path in to PEDOT:PSS, the model will still be able to converge.

As mentioned, the non-local TAT is facilitated by trap containing material. The goal of the trap state distribution in PEDOT:PSS was not to mimic the actual subgap energy states in the material, as not

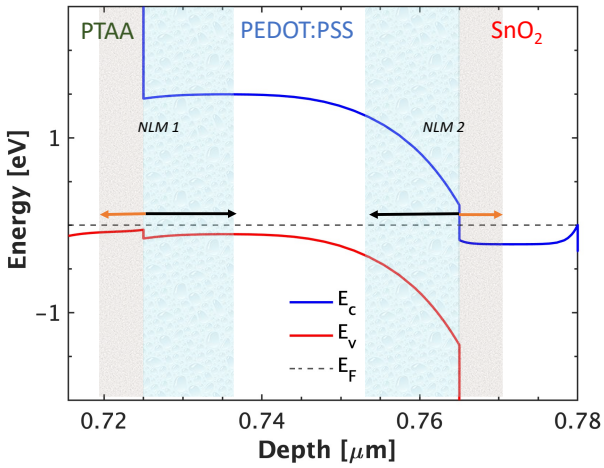

Figure 3.8: An example of the two needed non-local meshes that contribute to the non-local TAT mechanism [4, 71]. Each is implemented on the layer's interfaces where the TAT occurs (PEDOT:PSS). Length and permeation not to scale.

much is known for this material specifically, but rather to facilitate the TAT mechanism with a possible realistic energy distribution.

In the model a uniform distribution was added, acceptor-like and donor-like to bring computing time and complexity down. After a successful TAT implementation was observed, a more naturally occurring distribution was used: gaussian. A trap state energy close to the quasi Fermi level in PEDOT was chosen to enhance the effect of the trap states on the capture and emission mechanism described in chapter 2. SDEVICE models the non-local tunneling to traps as the sum of an elastic [52] and inelastic, photon-assisted process [72] where only the first one is considered as explained in section 2.3.

3.5. Model calibration

In the following section, the parameter calibrations of three different models are described. To fit the modelled J-V curves with experimental values, changes in the input parameters can be made, however, the changes should be inline with literature or experimentally obtained values.

3.5.1. Perovskite calibration

For the calibration of the perovskite single-junction multiple variables needed to be explored as literature and experimental in-house measurements could result in conflicting values for parameters. An important note for the perovskite single-junction is that the illumination during experimental measurements and for the opto-electrical model is done from the SLG side, making the cell in question a p-i-n architecture, see chapter 1.

The starting point of the calibration were the experimental obtained values for the used materials like approximate thicknesses of each layer and in-house measured electrical parameters in the single-junction. The optical measurements of the complex refractive index were extracted in-house. Literature research was needed for electrical parameters that could not obtained with the in-house measurements. For all materials in the tandem configuration, a database for the electrical parameters was created. The most important parameters were X, E_g, ϵ_R, N_c, N_v and μ. As many material properties are dependant on their production method, exact composition and measurement technique, fluctuating values were found.

To reduce the complexity of modelling, the first simulation were based on an ideal operating single-junction, not including trap state densities. Step one was convergence of the model. Using the simulated band diagram in equilibrium, convergence issues could often be contributed to band offset forming a barrier prohibiting charge carrier collection resulting in a non-functioning solar cell. This issue was often resolved by altering the parameter values for bandgap or electron affinity by other found values in the created database. The materials related to the main issues were found to be PTAA and PCBM. Adjustments eventually resulted in a proper band alignment with good charge carrier separation and collection.

Table 3.4: Material and device parameters of the top layer of the opto-electrical tandem model which includes the perovskite absorber layer. The abbreviation f SnO_2 refers to the front SnO_2 layer. CB DOS and VB DOS represent the density of states of conduction band minimum and valance band maximum, respectively.

Top Layer						
Layer parameters	Symbol [unit]	ITO	f SnO_2	PCBM	Perovskite	PTAA
Thickness	d $[nm]$	180	45	40	450	10
Bandgap	E_g $[eV]$	3.7	3.6	1.6	1.6	3.3
Electron affinity	χ $[eV]$	4.9	4.25	4.3	3.9	1.8
Rel. permittivity	ϵ_R	3.5	10	3.0	6.5	3
Doping	N_A,N_D $[cm^{-3}]$	$2.0{*}10^{20}$	$3.0{*}10^{18}$	$7.0{*}10^{17}$	$1.0{*}10^{16}$	$1.0{*}10^{18}$
CB DOS	N_C $[cm^{-3}]$	$4.1{*}10^{18}$	$4.0{*}10^{18}$	$2.2{*}10^{19}$	$1.0{*}10^{20}$	$2.2{*}10^{18}$
VB DOS	N_V $[cm^{-3}]$	$1.7{*}10^{19}$	$1.0{*}10^{18}$	$1.8{*}10^{18}$	$1.0{*}10^{19}$	$1.8{*}10^{19}$
Mobility	μ_e, μ_h $[cm^2/Vs]$	45,40	1E-3,0.25	4E-4,4E-4	35,35	4E-5,4E-5
Source	-	[61, 73]	[6, 61]	[74]	[6, 75, 76]	[49, 77]

The integration of the described spatial distribution of trap states density (subsection 3.3.4) was done in the last step. This increased the complexity of the single-junction model and resulted in effect on the external parameters of the solar cell and was used to calibrate the cell. As the results of Ni et al. [5] was based on thin-film Psc single-junction with different materials, compositions and productions methods, some freedom could be taken in interpreting the trap densities in the bulk and interfaces while remaining in the order of magnitude found in the paper. A summary of the eventually used parameters can be seen in table 3.4 and subsection 3.3.4.

3.5.2. CIGS calibration

The CIGS bottom layer used is a commercially fabricated solar cell. As the exact production method is unidentified, parameters like the thicknesses of the materials are unknown. Thus, a slightly different approach was used for the calibration of the cell. First, an ideal cell was modelled, using the same path as described for the perovskite single-junction. After electrical parameters were chosen that were comparable to literature values and resulted in a functioning CIGS single-junction, the spatial bandgap gradient model was introduced into the CIGS absorber layer.

Table 3.5: A summary of the most important material and device parameters of the bottom layer of the opto-electrical baseline tandem model including the CIGS absorber layer. The graded bandgap and electron affinity are explained in subsection 3.3.3.

Bottom Layer				
Layer parameters	Symbol [unit]	i-ZnO	CdS	CIGS
Thickness	d $[nm]$	45	40	$2.5{*}10^{3}$
Bandgap	E_g $[eV]$	3.3	2.4	Graded
Electron affinity	χ $[eV]$	4.3	4.2	Graded
Rel. permittivity	ϵ_R	9	10	13.6
Doping	N_A,N_D $[cm^{-3}]$	$1.0{*}10^{17}$	$8.0{*}10^{16}$	$2.0{*}10^{16}$
CB DOS	N_C $[cm^{-3}]$	$3.0{*}10^{18}$	$1.3{*}10^{18}$	$6.8{*}10^{17}$
VB DOS	N_V $[cm^{-3}]$	$1.7{*}10^{19}$	$1.0{*}10^{19}$	$1.5{*}10^{19}$
Mobility	μ_e, μ_h $[cm^2/Vs]$	100,30	72,20	100,12.5
Source	-	[66]	[66, 78, 79]	[66, 80]

The calibration of the CIGS single-junction was mostly achieved by adjusting the thicknesses of layers resulting in adaption of the found external parameter values. Due to possible different deposition parameters and fluctuating absorber thicknesses, the bandgap grading was unknown. Thus, by altering the values and parameters described in subsection 3.3.3 a fitting with the experimental data could be made. The eventual parameters can be found in table 3.5 and subsection 3.3.3.

Table 3.6: Material and device parameters of the tunnel recombination layer of the opto-electrical baseline tandem model. The m SnO_2 refers to the middle SnO_2 layer.

Tunneling Recombination Layer			
Layer parameters	Symbol [unit]	PEDOT:PSS	m SnO_2
Thickness	d $[nm]$	40	15
Bandgap	E_g $[eV]$	1.6	3.6
Electron affinity	χ $[eV]$	3.6	4.0
Rel. permittivity	ϵ_R	3	10
Doping	N_A,N_D $[cm^{-3}]$	$1.1*10^{18}$	$5.0*10^{19}$
CB DOS	N_C $[cm^{-3}]$	$2.2*10^{18}$	$4.0*10^{18}$
VB DOS	N_V $[cm^{-3}]$	$1.8*10^{19}$	$1.0*10^{18}$
Mobility	μ_e, μ_h $[cm^2/Vs]$	100,100	15,15
Source	-	[81, 82]	[6, 61]

3.5.3. Tandem calibration

As was shown in section 3.4, the band alignment which is mostly dependant on the doping concentration of the materials that are part of the TRJ can have a significant influence on the result of the tandem model after the implementation of TAT. Figure 3.2 shows the flowchart used for modelling the tandem cell, and states that material parameters used in the validation of the single-junctions are direct input for the tandem cell.

This leaves only the added PEDOT:PSS material as unknown input in the last part of calibration. The approach used is as following: First a tandem model template was made in TCAD Sentaurus including the single-junctions models containing the added trap distributions in both layer and bandgap grading in the CIGS absorber layer and the addition of the PEDOT:PSS material. Secondly, PEDOT:PSS was added to the material database and research was done on the possible different values for the electrical parameters. After that, the TAT model was implemented in the PEDOT:PSS layer. Lastly, the electrical parameters, mainly the doping concentration (N_A), was tweaked resulting in table 3.6. The results of the calibration will be shown in the next chapter 4.

4

Optical and Electrical bottlenecks

In Chapter 3 the methodology to obtain the baseline tandem cell was explained which will be used for the loss analysis in the the perovksite/CIGS tandem cell. In order of the proposed thesis approach, first the single-junctions solar cells will be validated in section 4.1. Secondly, the results for the trap assisted tunneling implementation in the TRJ can be viewed in section 4.2. This was used for the validation of the baseline tandem cell (section 4.3). All values regarding recombination mechanisms were extracted from the Sentaurus TCAD model. This resulted in a breakdown of the different losses in the cell in section 4.4. Lastly, a thorough analysis is done on the transport issues in the TRJ (section 4.5).

4.1. Validation single-junctions

This section presents the validation of the simulation template to confirm that the models reproduce the inner physics occurring in the fabricated baseline solar cells. For both cells the J-V curves were produced and compared to experimental measured data.

4.1.1. Perovskite single-junction validation

The Perovskite single-junction layer stack used for the optical and electrical model is seen in figure 4.1a. The illumination of the solar cell came from the SLG side of the stack, thus the cell technically has a p-i-n orientated configuration. Once introduced as top layer in the tandem stack, the cell resides as a n-i-p configuration with illumination from the ETL (PCBM) side. Figure 4.1b shows the comparison between the measured and simulated J-V curve for the reference sample under AM1.5 illumination. Table 4.1 gives an overview of the found external parameters (J_{sc}, V_{oc}, PCE and FF). Overall a good corresponding fit between the experimental and simulation was achieved. However, the simulation shows a slightly underestimated current density (0.3 mA/cm^2) and overestimated FF of about 1.75%.

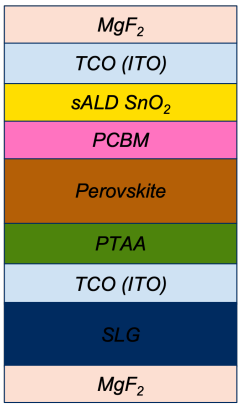

(a) The Perovskite single-junction layer stack used for calibration of the opto-electrical Perovskite model. The layer thicknesses and materials compositions are similar to the ones used in the tandem cell top layer. The illumination is coming from SLG side.

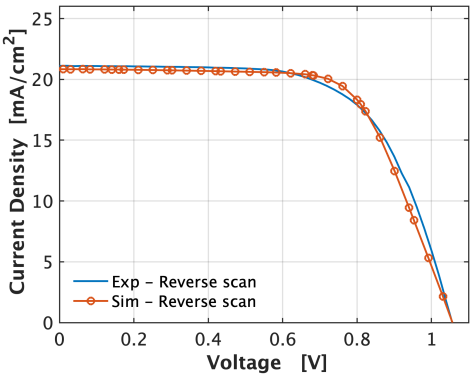

(b) The J-V curve obtained from the opto-electrical single-junction Perovskite model vs. the experimental J-V curve.

Figure 4.1

The band diagram in figure 4.2 shows similar characteristics and band alignments as reported in the literature for the PTAA/perovskite/PCBM system [74]. The SnO_2 layer in figure 4.2 (green layer) exhibits band offsets at both interfaces of 0.51 eV at PCBM/SnO_2 and 0.65 eV at SnO_2/ITO. Further

discussions about the effect of these band offsets on the functioning of solar cell are presented in chapter 5.

The model reproduces measured J-V curves with only minor differences for the external parameters and therefore gives a representation of the inner physics in the perovskite solar cell.

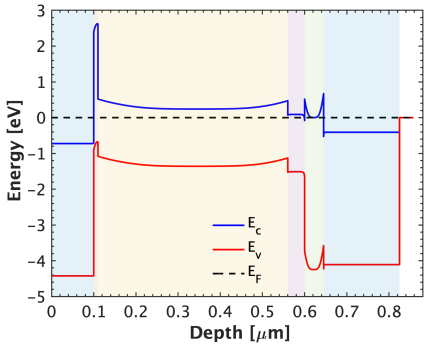

Figure 4.2: The obtained band diagram of the pervoskite single-junction model in the dark with no applied voltages. Note the illumination is coming from the ITO/PTAA side on the left.

4.1.2. CIGS single-junction validation

For the single-junction, the layer stack, seen in figure 4.3a was modelled. This CIGS stack was ultimately used as the bottom cell for the tandem model.

Figure 4.3b shows the comparison of the obtained J-V curves for experimental and simulated results. A reasonable match between the simulated and measured curves can be identified, which is also seen in the simulated and external parameters found in table 4.1. The V_{OC} of 0.692 has a negligible overestimation of 0.004 V. A similar deviation of 0.002 mA/cm^2 is obtained for the J_{SC}. We concluded that the simulation template accurately reproduces experimentally obtained J-V curves and thus the physical mechanics in the CIGS bottom cell. This indicates a valid model that can be used as the bottom part of the tandem model.

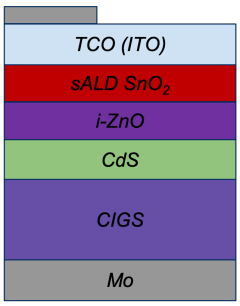

(a) The CIGS single-junction layer stack used for calibration of the CIGS opto-electrical model. The layer thicknesses and materials compositions are similar to the ones used in the tandem cell bottom layer.

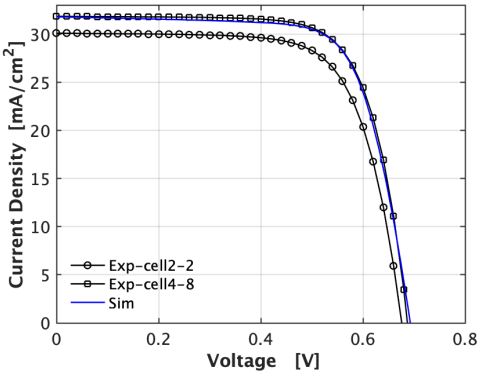

(b) The J-V curve obtained from the opto-electrical single-junction CIGS model vs. the experimental J-V curve.

Figure 4.3

4.2. Results of TAT implementation

After validation of the physical mechanisms inside the perovskite and CIGS single-junction model templates, the next step is the validation of the perovskite/CIGS tandem model. To further develop the simulation model, one should first analyze the transport mechanisms in the TRJ. The previous chapter hinted at the possibility of the TAT mechanism occuring in the TRJ, and how to implement this in the

Table 4.1: A comparison of the most important external parameters (Jsc,Voc, FF and PCE) of the single-junction model results to the experimental data. The experimental values were obtained from in-house measurements [61].

External parameters	V_{oc} $[V]$	J_{sc} $[mA]$	FF	PCE [%]
Perovskite exp	1.051	21.11	64.33	14.34
Perovskite sim	1.052	20.83	66.08	14.45
CIGS exp	0.688	31.80	72.05	15.76
CIGS sim	0.692	31.82	72.09	15.89

model. In this section the results are shown.

A TRJ consists of two regions, a p-type region and a n-type region. The TAT mechanism is dependant on the band alignment within this two regions. This band alignment can be described as the energy difference in the band diagram between the VB in the p-type region and the CB in the n-type region, which is referred to as ΔE. In the baseline tandem cell this is defined as the energy level of the SnO_2 layer's CB (E_{CB,SnO_2}) minus the energy level of PEDOT:PSS ($E_{VB,PEDOT:PSS}$).

A higher value of ΔE indicates a higher energy barrier for the transport of charge carriers [71]. In figures 4.4a, 4.4b and 4.4c different band diagrams are shown, each with a different value of ΔE. For this section, the ΔE is altered by changing the doping concentration in the SnO_2 layer while keeping the PEDOT:PSS doping constant. Figures 4.4a and 4.4b show a positive value ($0.15eV$ and $0.1eV$, respectively) indicating a misalignment of the CB and VB.

Figure 4.5a shows the J-V curve for the cases: a) ΔE = 0.15, b) ΔE = 0.10, and c) ΔE = -0.10. The result of this is shown in figure 4.5a. The simulation results and the experimentally obtained J-V curve are shown. The J-V curve for the values 0.15 and 0.1 eV present similar results, with J_{sc} being 10.36 mA/cm^2 versus the experimental 11.36 mA/cm^2 and a clearly lower V_{oc} compared to the reference cell (0.55 V vs. 1.56 V). For the negative value of ΔE = -0.1eV, the results show a value of 12.16 mA/cm^2 and 1.662 V. The J-V curve observed for 0.15 and 0.1 eV (figure 4.5a, yellow line) show a minor functioning cell when compared to ΔE = -0.1 (4.5a, blue line).

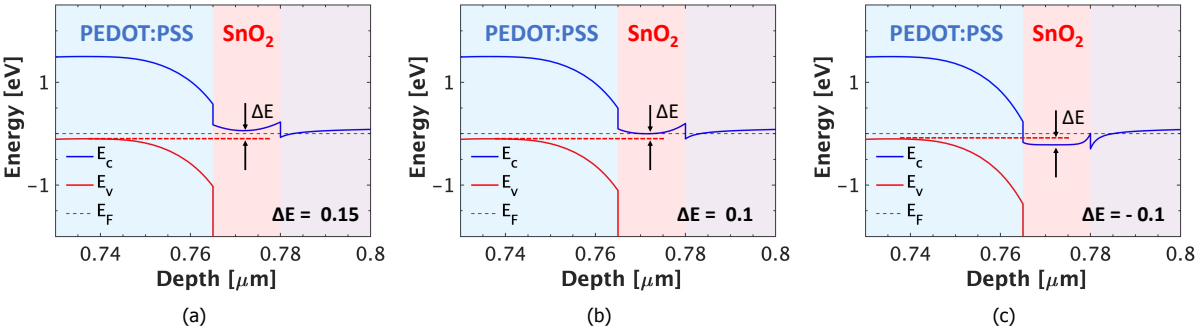

Figure 4.4: The TRJ for different values of ΔE

Figure 4.5a shows that direct tunneling, which is the direct energy transition of charge carrier via B2BT, is not able to accurately reproduce the experimentally obtained results. Consequently, TAT is implemented, which facilitates indirect energy transitions via trap states (the mechanisms are visualised in figures 3.7a and 3.7b).

Figure 4.5b shows the results for the model with the same three band alignments (0.15, 0.1, and -0.1 eV) of the CB_{SnO_2} and $VB_{PEDOT:PSS}$ after the implementation of the mid-gap Gaussian trap distribution in PEDOT:PSS and the TAT. To illustrate the effect of the TAT mechanism, the outcome of the simulation for ΔE = 0.15 eV in both figure 4.5a and 4.5b are compared. The possibility of the TAT mechanism happening in the model in figure 4.5b is evident as the J-V curve is significantly improved, even when B2BT is not possible anymore due to misalignment of the CB_{SnO_2} and VB_{PEDOT}. When comparing the cell characteristics for ΔE = 0.15 eV, the J_{sc} improved from 10.36 mA/cm^2 to 11.96 mA/cm^2, V_{oc} from 0.533 V to 1.542 V and the FF from 33.64 to 53.02. The J-V curves for different ΔE values, show a less performing cell with increasing ΔE which will be further discussed in section 4.5.

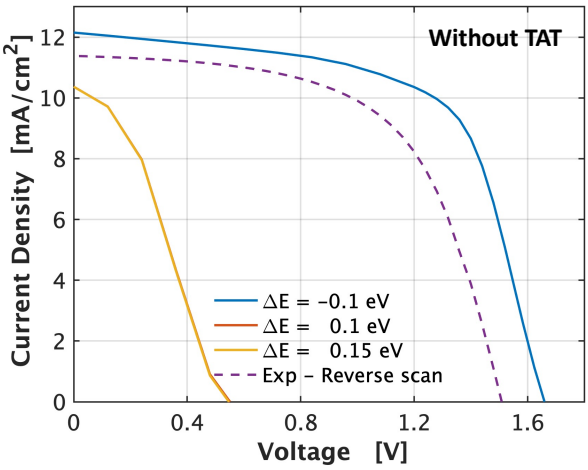

(a) The outcome of simulation model for different ΔE values without the implementation of trap assisted tunneling compared to the experimental values of the tandem cell.

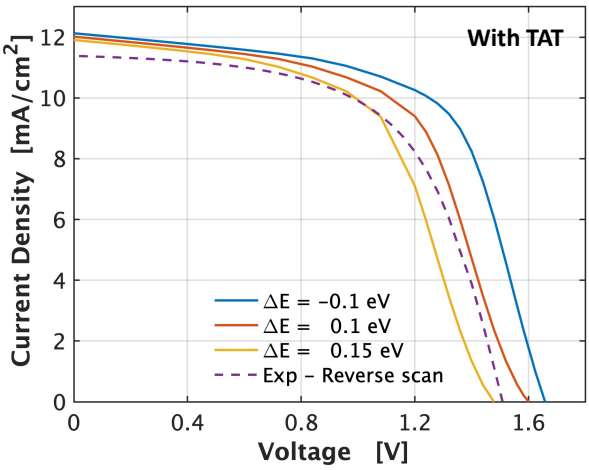

(b) The outcome of the simulation model for different ΔE values with the implementation of trap assisted tunneling compared to the experimental values of the tandem cell.

Figure 4.5

This section showed the successful implementation of TAT mechanisms via defects distributed as a Gaussian curve in the forbidden energy domain in the PEDOT:PSS layer, resulting in the possibility to alter the results for the cell characteristics of the tandem cell model by only changing TRJ parameters. It was demonstrated that transport of charge carriers through the TRJ is based on two different tunneling mechanisms, B2BT and TAT. In the next section this will be used to validate the tandem model.

4.3. Tandem cell validation

After validation of the two single-junction and the successful TAT implementation, we move to the validation of the perovskite/CIGS tandem cell. The modelled layer stack is seen in figure 4.6a which shows the similarity with the two single-junction layer stacks used in previous sections.

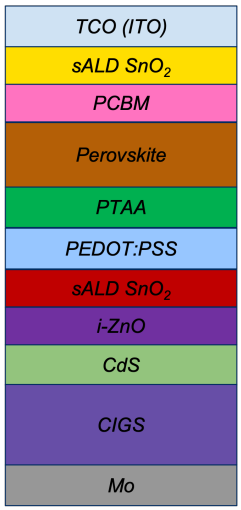

(a) The material layer stack of the baseline perovskite/CIGS tandem cell.

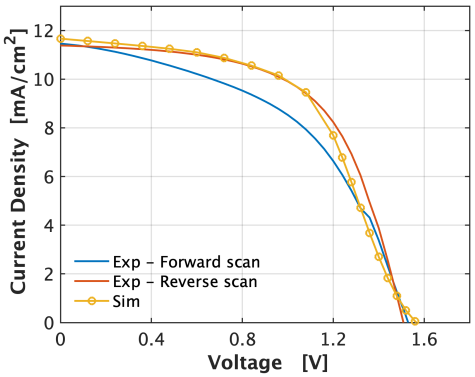

(b) Four terminal architecture with two separate subcells. Although less sensitive to spectral variation, extra layers and cabling are needed [19].

Figure 4.6

Again, the J-V curves under 1.5AM illumination for the experimental and modelled results were compared in figure 4.6b. For the experimental results the forward and reverse scan can be observed (figure 4.6b, blue and red line, respectively), showing a difference in obtained curves due to the

Table 4.2: A comparison of the most important external parameters (Jsc,Voc, FF and PCE) of the tandem model results to the experimental data. The experimental values were obtained from in-house measurements [61].

External parameters	V_{oc} $[V]$	J_{sc} $[mA]$	FF	PCE [%]
Tandem exp reverse	1.509	11.38	59.33	10.19
Tandem exp forward	1.529	11.46	48.94	8.58
Tandem sim	1.567	11.94	56.90	10.63

hysteresis effect in the perovskite top layer. The model was calibrated to the reverse scan. The reverse scan and simulation show a similar shape profile from 0 to 1.1 V. Thereafter, an s-shape behaviour is observed when moving closer to the V_{OC}.

Table 4.2 gives an overview of the obtained external parameters. The values for the forward scan are stated, but only the comparison between the experimental and reverse scan will be used for the validation. An overestimation of the V_{OC} by 0.058 V was seen for the model, which could mainly be contributed to the s-shape of the J-V curve nearing the V_{OC}. A difference in J_{SC}, 11.38 versus 11.94 mA/cm^2, was seen. As the J_{SC} is mostly dependant on the optical generation and to less extent on the electrical parameters and carrier transport, the difference in values was considered to be acceptable as the top and bottom layer thicknesses can not be altered. Changing the thickness of an absorber layer would have effect on the validated single-junction models. The FF was found to be 3 percentage points lower than the experimental reverse scan, and can mainly be contributed to the s-shape near the V_{OC}.

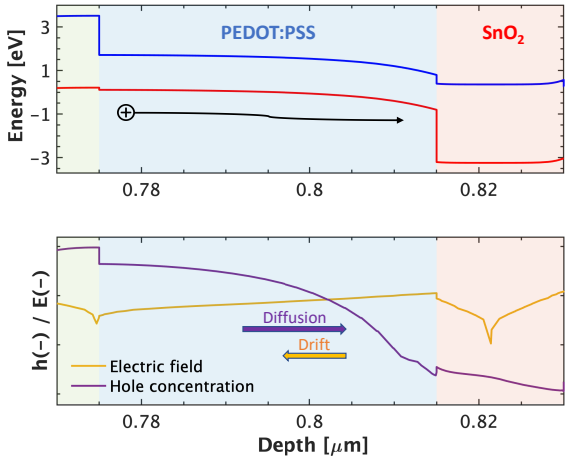

Figure 4.7: The electric field (E) and hole concentration (h) in the PEDOT:PSS layer of the baseline tandem cell. The magnitude of both parameters are normalised values and not to scale.

The tandem model is validated as it can reasonably reproduces the J-V curve. Therefore, it replicates the physical mechanisms of the perovskite/CIGS tandem cell. The model can thus be used to calculate the losses and analyze the charge carrier transport in the TRJ of the reference baseline tandem cell.

However, an s-shape was observed in the J-V curve produced by the model template. The s-shape could result from two reasons: 1. The increased energy barrier for charge carriers to tunnel through the TRJ via TAT, as energy level change needs to occur when hopping from trap to trap. 2. Strong band bending in the PEDOT:PSS layer towards the PEDOT/SnO_2 interface leading to a opposing drift current for holes away from the TRJ, see figure 4.7. The figure shows the electric field on a normalised exponential scale. The electric field increase exponentially towards the PEDOT/SnO_2 interface working against the hole transport towards the TRJ. As the exact difference in physical mechanism between the reference baseline tandem cell and the model is unclear in this region, further research would be needed to improve the reproduction of the experimental J-V curve by the model and remove this s-shape.

4.4. Baseline cell loss analysis

The obtained baseline tandem cell was used as reference for the loss analysis. The analysis were made at short circuit (SC) and maximium power point (MPP) conditions to better understand the arising effect of certain recombination mechanisms when operating the cell. This will give more insight in the existing losses (both optical and electrical).

4.4.1. Photocurrent distribution

The charge conservation principle states that the total amount of electric charge in a system does not change with time, thus all charge particles that are created must be collected at the electrodes or recombined in the cell. When every incoming photon from the incident light would create one charge charge carrier separation, the possible photo-current (J_{ph}) would add up to 46.45 mA/cm^2. Following the charge conservation principle, the total absorption and losses extracted from the tandem model should eventually add up to J_{ph}. Figure 4.8 shows the distribution of the J_{ph} in the reference tandem and shows the total photo-current accumulates to 46.45 mA/cm^2.

To give proper insights in the breakdown of the photo-current, a division was made in top cell, bottom cell, parasitic absorption and reflectance. It is important to mention that the values for top cell, bottom cell and parasitic absorption are not directly extracted from GENPRO4 but take in to account shading losses from the front contact (see the next subsection for more explanation).

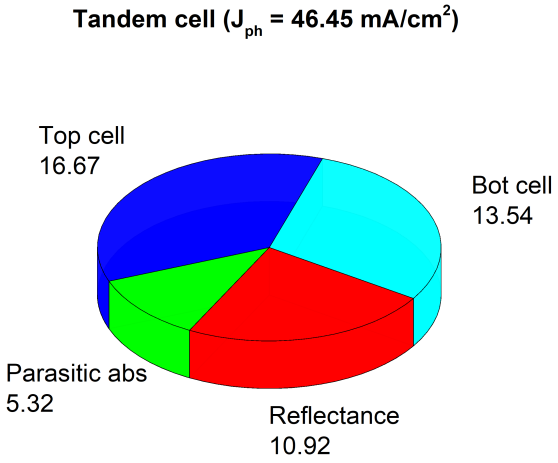

Figure 4.8: Breakdown of the total extracted photo-current density and the related reflection and parasitic absorption at short circuit conditions for the baseline Perovskite/CIGS tandem described in chapter 3. The top cell and bottom cell part include the J_{sc} and other loss mechanisms. All values are given in mA/cm^2.

Figure 4.8 presents a generated current density of 16.67 mA/cm^2 in the top cell and 13.54 mA/cm^2 in the bottom cell, which make up 65.0% of the J_{ph}. Reflectance contributes to the loss of 23.5% of the J_{ph}. This is about two times a high as the parasitic absorption, which totals to 5.32 mA/cm^2, this will be broken down further in section 4.4.2. The top and bottom cell current mismatch indicates an sub-optimal current density for the tandem cell as the lowest current density in top or bottom cell dictates the measured current density at the electrodes. Two factors have to be taken into account when discussing this phenomenon. First is the mismatch due to absorber thicknesses and secondly, the mismatch due to bandgap widths. Both will be discussed in more depth in section 4.4.5. The reflectance losses are very high, exceeding the average found reflectances for perovskite-based cells, which is around 10% on average [83] and will further be discussed in section 4.4.3.

4.4.2. Parasitic absorption

Parasitic absorption refers to the absorption of photons in non-absorber materials which do not eventually contribute to current density of the solar cell and can be considered as losses. In figure 4.9a the

contributors to the parasitic losses are visualised. The parasitic absorption has four main contributors that are responsible for 95% of the total parasitic absorption. The parasitic absorption due to the back contact of Molybdenum (Mo) is the largest contributor with 2.097 mA/cm^2, followed by front TCO (ITO) with 1.209 mA/cm^2, PCBM (0.942 mA/cm^2) and PEDOT:PSS (0.807 mA/cm^2). A possible increase of +11.4% of the J_{SC} could be obtained by reducing these current density losses.

The Molybdenum has a high absorption coefficient, combined with the low reflectivity of the material, resulting in significant absorption of the incoming photo-current. This absorbed light cannot contribute to charge carrier generation in the absorber layers [22]. This is a known issue and search for different materials is ongoing [84], however, so far Mo exhibits the best properties.

As the front TCO layer acts as transport medium, window layer and anti-reflection coating, concessions have to be made regarding material choice as a material is not able to perform optimal on all three aspects. Bandgap absorption is observed for wavelengths below 450 nm [85] and can be optimized by altering the potential doping, pushing the absorption to lower wavelengths due to filling of states in the bottom of the conduction band due to the Burstein-Moss effect [86]. This would result in reduction of parasitic absorption as less photons will be absorbed due to an increased bandgap. This could potentially lead to an increase in current density created in the perovskite top layer as it absorbs light in the spectrum between 300-800 nm.

Parasitic light absorption in the sun-facing front molecular layer is known to cause lower PCE. The PCBM layer absorption spectrum is situated between 0 and 550 nm. As an important role of PCBM is the electrical transport of created charge carriers in the perovskite bulk layer, changing the material for a material with less parasitic absorption could have a negative effect on the functioning of the solar cell. A material with a larger bandgap could reduce the parasitic absorption, however, the change in electrical parameters could affect the charge carrier transport. Transport issues could occur due to changes in the energy alignment in the band diagram, potentially creating band offsets. According to Jacobsson et al. [2], PCBM remains the most prominent candidate as it is the most frequently used material in perovskite stacks. However, a similar material, C60, that could potentially lead to an electrical enhancement of the cell, seems to result in higher parasitic absorption [87].

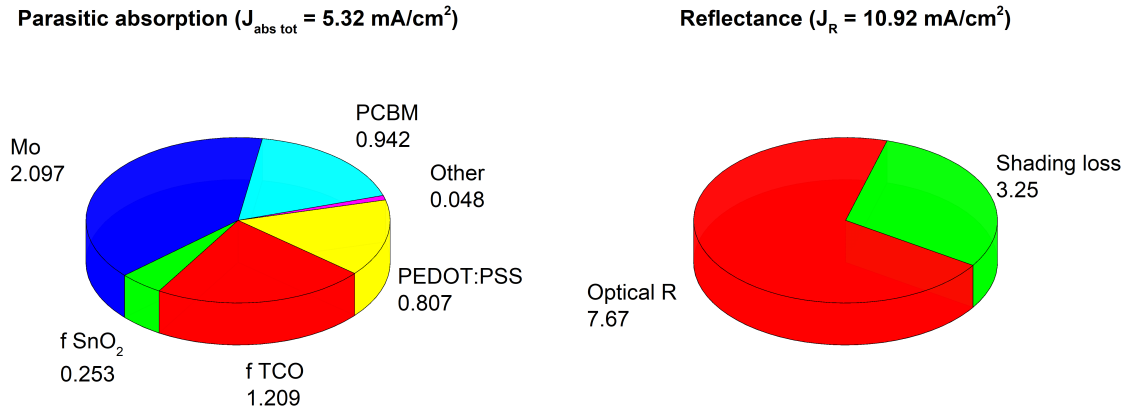

(a) An overview of the layers contributing to the parasitic absorption in the baseline tandem cell. Mo refers to the Molybdenum back contact. The f indicates the layer is situated on the front side of the cell. All values are given in mA/cm^2.

(b) An overview of the reflectance losses including optical reflectance (Optical R) and shading losses due to the metal contact on the front of the cell. All values are given in mA/cm^2.

Figure 4.9

4.4.3. Reflectance

The losses due to reflectance are divided into two parts: optical reflectance and shading losses (also known as metalisation). Not all incoming light can reach the cell as a metal front contact blocks an area from the irradiance. The illumination window (IW) is the area of the cell that can be reached by the incoming light.

To calculate the optical reflectance, equation 4.2 was used. The optical reflectance equals the reflectance obtained from GENPRO4 multiplied by the illumination window (IW) ratio to the total width of the cell (W_{IW}/W_{tot}) as the cell is modelled in 2-D, and equals 0.93 (see section 3.4. This results in a $R_{optical}$ of 7.67 mA/cm^2.

$$W_{tot} = W_{IW} + W_{contact} \tag{4.1}$$

$$R_{optical} = J_{R,GenPro} * \frac{W_{IW}}{W_{tot}} \tag{4.2}$$

$$R_{shading} = J_{ph} * \frac{W_{contact}}{W_{tot}} \tag{4.3}$$

The shading loss is dependant on the width of the contact in ratio to the total width. The shading loss equals the irradiance that cannot reach the cell and is thus dependant on the width of the contact and the incoming J_ph. Equation 4.3 is used to calculate the shading loss. The shading loss is found by multiplying the coverage factor ($W_{contact}/W_{tot}$), times the J_{ph}. This is results to 3.25 mA/cm^2. The shading losses can be reduced by making the front contact area as small as possible.

In Santbergen et al. [60] it was shown for a Perovskite/c-Si tandem that the interfaces in the front layers of the cell cause a significant reflectance in the whole wavelength spectrum. This reflectance originating from the interfaces can be reduced by applying a standard anti-reflective coating on top of the ITO [60]. A significant improvement in absorption of photons was seen for perovskite/CIGS tandem cells with the addition of dielectric nano-cone structures on the top layer [88]. This research suggests that an addition to the front side of the tandem cell could result in significant changes in the reflectance.

4.4.4. Top cell losses

For an assessment of the losses in the top (perovskite) and bottom cell (CIGS), an analysis was done in SC condition and at the MPP. The difference in values for recombination current in SC conditions and MPP shows the effect of recombination mechanisms on the FF of the device. The increase of recombination when comparing SC with MPP, can be related to charge transport issues in the collecting path of charge carriers.

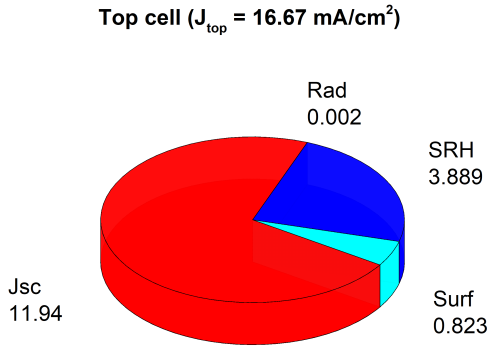

(a) Overview of the main recombination mechanisms contributing to the recombination current density in the top cell in SC conditions. All values are given in mA/cm^2.

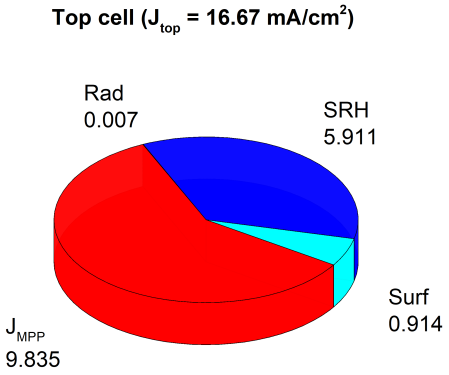

(b) Breakdown of the current density distribution on the top cell at MPP. All values are given in mA/cm^2.

Figure 4.10

Figures 4.10a and Figure 4.10b present the results for the top cell recombination losses in SC and MPP conditions, respectively. Both figures show the contribution to the losses in the top cell can mainly be contributed to SRH recombination, which increases when operating in MPP (3.889 mA/cm^2 to 5.911 mA/cm^2). This is 23% of the total absorbed current density in the top cell. Radiative recombination

(Rad), although perovskite can be described as a direct bandgap material, seems to be an insignificant contribution to the recombination losses (around 0%). The last main contributor to recombination in the top layer is surface recombination (Surf) at the interfaces of the perovskite layer with the HTL and ETL which is equal to 0.823 mA/cm^2 for J_{SC} and 0.914 mA/cm^2 in the MPP (light blue, figures 4.10a and 4.10b).

It is reported that trap-assisted recombination (SRH recombination) is the main contributing loss mechanism in perovskite solar cells (PSCs), which is in line with the obtained results [89, 90]. As the SRH recombination occurs through states within the bandgap, the Fermi level of the absorber layer has a significant influence on the recombination rate, as highly doped materials result in higher recombination rates. Trapping in materials with an excess of charge carriers will result in immediate recombination as the trap states may already be filled with opposing carriers due to trapping.

A second non-radiative recombination (surface recombination) takes place at the interfaces of the perovskite layer where, according to our model (see section 3.3.4), an increase in trap state density is observed, both at the HTL and ETL interface. Interface recombination is well known to impact the external properties of perovskite solar devices [91, 92]. Non-radiative recombination losses can lead to non-radiative V_{OC} losses which can directly effect the FF.

The path for a charge carrier to an electrode can be seen as a series resistance, less resistance results in faster transport towards the electrodes, minimizing the change of recombination. As the applied voltage increases, less charge carriers are able to meet the required voltage to be collected at the electrodes ($V_{carier} > V_{electrode}$). The applied bias (potential) shrinks the collection of free carriers, accordingly the free carriers' density inside the cell increases with the consequent reduction of the band bending leading to recombination of the charge carriers in the absorber material. Thus an improved charge transport towards the electrodes reduces the resistance, resulting in less recombination and a better functioning cell.

The figures 4.10a and 4.10b show the importance of minimizing the surface and bulk non-radiative recombination losses. Several techniques can be used to reduce the surface and bulk recombination: 1) Reducing and passivating the trap sates at the interface and bulk and 2) improving the carrier transport towards the electrodes. A reduction in recombination will positively affect the external parameters of the reference solar cell [93, 94].

4.4.5. Bottom cell losses

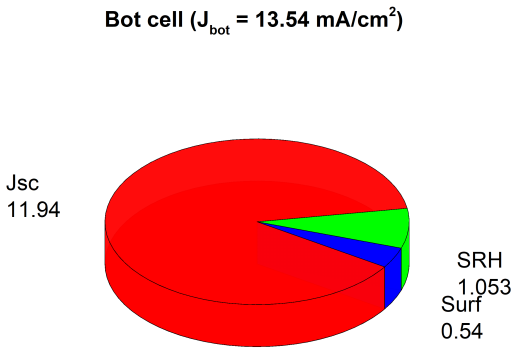

(a) Breakdown of the current densities the CIGS bottom cell in SC conditions. All values are given in mA/cm^2

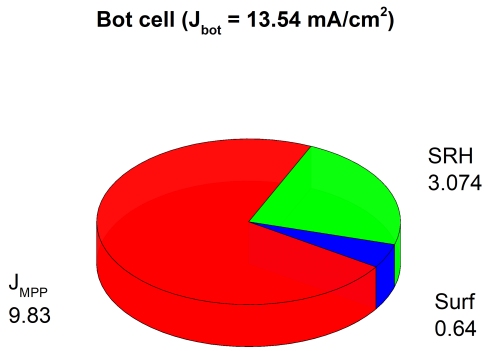

(b) Summary of the found current densities in the CIGS bottom cell at MPP. All values are given in mA/cm^2

Figure 4.11

Figure 4.11a and 4.11b show the obtained loss analysis in the bottom cell of the tandem stack. As expected, the J_{SC} and J_{MPP} are similar to the values in the top cell as the currents are matched in both layers, 11.94 and 9.83 mA/cm^2 respectively. The polycrystalline nature of the CIGS lead within the model to the introduction of a significant concentration of trap states: $5*10^{13}$ $/cm^3$. This facilitates SRH recombination in the bulk which can be seen in the results as the dominant recombination mechanism (1.053 mA/cm^2) and is in line with literature [95]. Surface recombination is observed (0.54 mA/cm^2),

which is also a defect-induced recombination mechanism by dangling bonds at the interfaces of the absorber layer, caused by the defects at the CdS/CIGS interface [95].

The contribution of the recombination losses in CIGS is 10.9 %, compared to the 28.3 % in the top cell. This difference in non-radiative recombination losses is contributed to the difference in trap state densities in both layers which is 10 times higher in the bulk of perovskite and even more towards the interfaces (2 to 3 orders of magnitude).

The figures 4.10a and 4.11a show the current limiting characteristics of the bottom cell, as the total generated current in the top layer is 2.23 mA/cm^2 higher. The overall tandem current will thus be limited by the CIGS bottom cell. This could be solved by altering the thicknesses of the absorber layers which will be discussed in chapter 5 or a potential bandgap modification in the CIGS layer by lowering the GGI value.

4.5. Transport evaluation of the TRJ

Results in section 4.2 show the effect of the band alignments in the TRJ on the functioning of the cell. In this section, the effect of the transport through the TRJ on the external parameters of the solar cell will be presented. By adjusting parameters that contribute to the alignment in the TRJ, insights on the charge carrier transport and induced recombination in the TRJ are extracted.

To evaluate the TRJ charge carrier transport, the parameters that are related to the alignment of the VB in the p-type material and the CB in the n-type layer are studied. As explained before in section 4.2, the band alignment can be described with parameter ΔE. ΔE can be explained in terms of two parameters related to the Fermi level in the TRJ.

Figure 4.12 visualises these parameters in the PEDOT:PSS and SnO_2 junction. In the PEDOT:PSS and SnO_2 layers, the energy difference between the Fermi level and the closest energy band is ascribed to the total energy misalignment via equation 4.4. Following equations 4.5 for the n-type region (SnO_2) and 4.6 for the p-type region (PEDOT:PSS), a relationship between this band alignment parameters and the doping can be found. High doping concentrations result in low values for the parameters. To study the effect of ΔE, the doping in both layers are changed resulting in different band alignments.

$$\Delta E = (E_F - E_V) + (E_C - E_F) \tag{4.4}$$

$$\Delta E_n = E_C - E_F = k_B T \ln\left(\frac{N_C}{N_D}\right) \tag{4.5}$$

$$\Delta E_p = E_F - E_V = k_B T \ln\left(\frac{N_V}{N_A}\right) \tag{4.6}$$

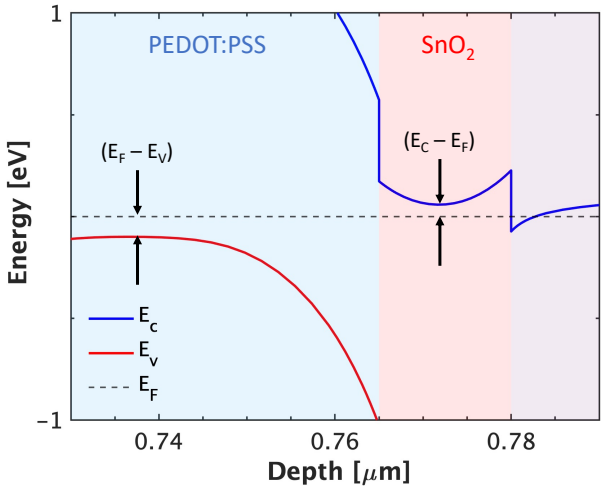

Figure 4.12: Visualisation of two band alignment parameters that were adjusted, $E_F - E_V$ (ΔE_p) for PEDOT:PSS and $E_C - E_F$ (ΔE_n) or for SnO_2.

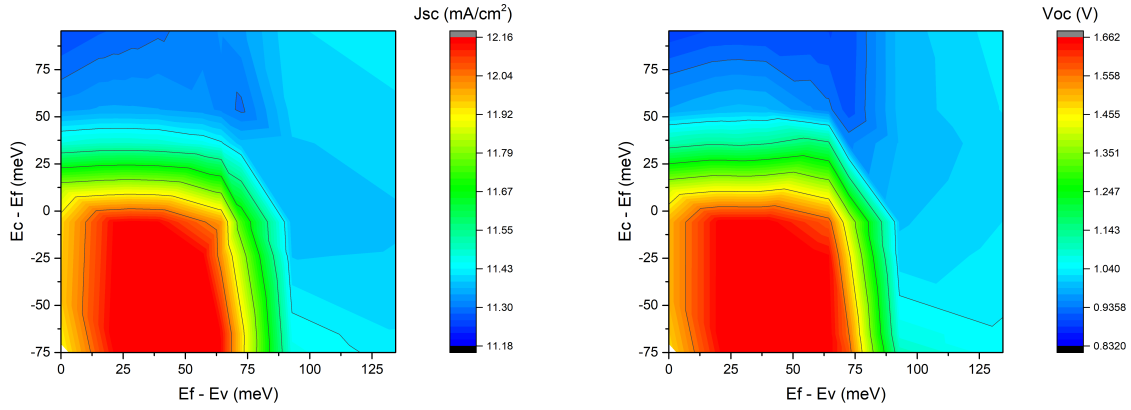

(a) The effect of band alignment parameters on the J_{SC}

(b) The effect of band alignment parameters on the V_{OC}

(c) The effect of band alignment parameters on the FF

(d) The effect of band alignment parameters on the PCE

Figure 4.13: The contourplots relating the value for ΔE_n $(E_C - E_F)$ in the SnO_2 region to the ΔE_p $(E_F - E_V)$ in the PEDOT:PSS region to external cell parameters of the tandem cell.

To understand the effect of different energy alignments on the external parameters of the modelled tandem, the doping levels were changed between concentrations that resulted in acceptable values for ΔE_n and ΔE_p. For the n-type region, the boundaries were set to -75 meV and 100 meV (SnO_2) and for the p-type, 0 meV to 135 meV (PEDOT:PSS), see figures 4.13. For the different energy values, simulations were run and the external parameters were extracted resulting in contour plots indicating the impact of the TRJ alignment on the V_{OC}, J_{SC}, FF, and PCE.

Figure 4.13 reports the simulated external parameters as a function of the band alignment. For the external parameters a minimum and maximum can be found. The lowest value for J_{SC} is 11.18 mA/cm^2 and the optimum is 12.16 mA/cm^2. For V_{OC} and the FF, the lowest values are 0.832 V and 42.20%, respectively. The highest found value for V_{OC} is 1.66 V, nearing the theoretical obtainable V_{OC} based on the single-junction cells (which is 1.743 V). For the FF, the optimum is 63.60.

The plots in figure 4.14 show the band diagrams for the PEDOT/SnO_2 junction for two different points in the contour plot: a) A point in the optimum region of the contour plot (red area, figure 4.13) and b) a point in contour plot resulting in minimum values for the external parameters (blue area, figure 4.13).

Figure 4.14a shows the band diagram for ΔE_n = -50 meV and ΔE_p = 25 meV, which is situated in the optimum region. The alignment of the $VB_{PEDOT:PSS}$ and the CB_{SnO_2} is observed. This means direct energy transfer of charge carriers is possible due to the B2BT. This efficient charge transport mechanism results in optimal values for the external parameters. Figure 4.14b shows the band diagram for ΔE_n = 0 meV and ΔE_p = 125 meV. On the contrary to figure 4.14a, a misalignment of of the $VB_{PEDOT:PSS}$ and

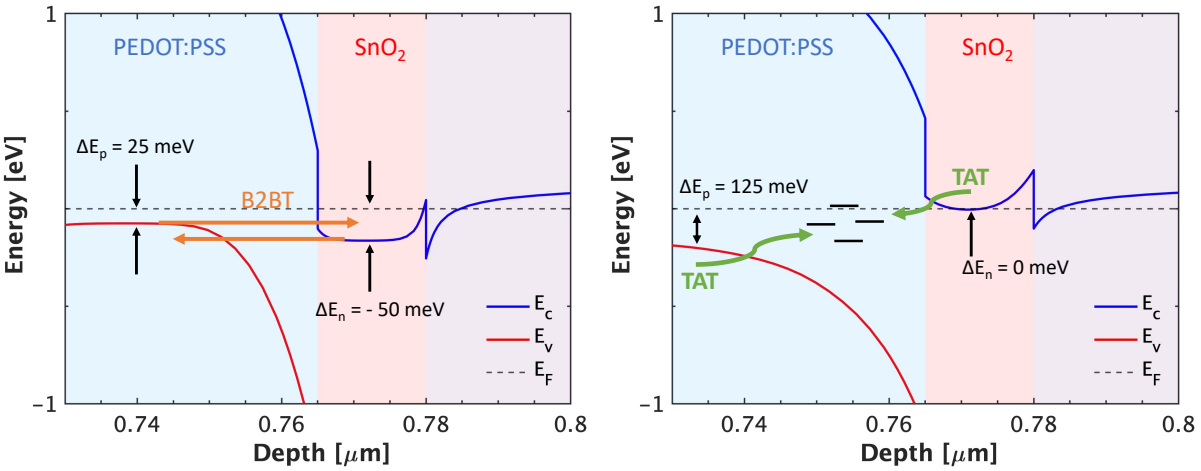

(a) The band diagram for ΔE_n = -50 and ΔE_p = 25, B2BT mechanism possible.

(b) The band diagram for ΔE_n = 0 and ΔE_p = 125, charge transfer dependant on TAT

Figure 4.14

the CB_{SnO_2} is observed. The charge transfer through or into the forbidden gap becomes dependant on the indirect energy transfer via trap-states with TAT. As this mechanism is less efficient for charge transport, it results in lower values for the external parameters compared to the optimum.

In the contour plot, the effect of transition from the TAT-dominated transport to B2BT mechanism can be observed for low values of ΔE_p ($12.5\ meV < \Delta E_p < 65\ meV$). This indicates highly p-type materials with the Fermi level close to the VB. For the n-type material in the TRJ, a highly doped material resulting in a negative value for ΔE_n is needed. This means that the Fermi level is inside the CB, which translates to highly conductive materials also known as a degenerate semiconductor. The SnO_2 already seems to exhibit these properties (see section 3.6).

Lastly, when combing the observed trends for the three previous external parameters, logically an overall improvement of the tandem device in the efficiency can be obtained. The results in figure 4.13d show significant differences in operational properties of the different TRJ configurations. The PCE for $(E_C - E_F) > 37.50\ meV$ and $(E_F - E_V)$-values between 0 and 75 meV is around 5%, while a potential of 12.84% is attainable. In figure 4.13d this is emphasised by the addition of the baseline tandem point. The baseline point shows the degenerate nature of SnO_2 which is, as previously discussed in section 4.5, a positive attribute. However, the VB positioning to the Fermi-level of PEDOT:PSS shows room for improvement and should be reduced by increasing doping or using a different material.

It should be noted that the analysis was done for a TRJ with a PEDOT:PSS and SnO_2 layer. The contour plots give a relation between ΔE value and the functioning the tandem cell for these specific materials. Introducing other materials could result in different optima as barrier potentials, band offsets and transport towards the TRJ induced by different electrical parameters can have effect on the transport in the TRJ. Meaning, a different optimum can be found for different material choices. This will be further discussed in chapter 5

4.6. Conclusions

In this Chapter, both single-junction models were successfully validated. It was found that transport in the TRJ of the tandem model of the reference tandem cell was based on two mechanisms: B2BT and TAT. After using a non-local TAT model facilitated by the implementation of a mid-gap Gaussian trap distribution in the PEDOT:PSS layer in the TRJ, the perovskite/CIGS tandem model was validated using the reference tandem cell. The losses in the reference cell were assessed and limiting aspect of the band alignment inside the TRJ was researched. This information will be used for possible improvements that will further improve the functioning of the tandem cell and is found in chapter 5.

5
The road to improvement

In chapter 4, the baseline tandem cell was analysed and flaws in the functioning of the cell were identified. This chapter will propose improvements that can potentially lead to higher efficiencies for the perovskite/CIGS tandem cell. The following four points will be addressed:

1. Improving carrier transport in the TRJ
2. Improving the optical properties of the reference cell
3. Improving carrier transport in the top layer
4. Reducing trap-state induced SRH recombination in the perovskite layer

In the first section (5.1), an alternative for the PEDOT:PSS material in the TRJ is presented. In section 5.2, an optical current match and overall optical improvement in the absorber layers are explored. In section 5.3, an optimization is proposed for the charge carrier transport in the top layer by altering the front SnO_2 material. The dominant recombination mechanism in the perovksite is tried to be reduced in section 5.4. In the last section of this chapter, all changes are implemented in the baseline tandem cell to see the effect on the external parameters and improve the efficiency of the cell.

5.1. The TRJ optimization

Chapter 4 showed the baseline tandem does not operate optimally due to limitation in the charge transport inside the TRJ. The contour plots indicated possible improvements in the p-type region, which is discussed in section 4.5. Accordingly, this section analyses the use of a different material for the p-type region.

Table 5.1: A comparison of PEDOT:PSS and NiO parameters for the TRJ

Material comparison			
Layer parameters	Symbol [unit]	PEDOT:PSS	ALD NiO
Bandgap	E_g $[eV]$	1.6	3.84
Electron affinity	χ $[eV]$	3.6	1.4
Rel. permittivity	ϵ_R	3	11.9
Doping	N_A,N_D $[cm^{-3}]$	$1.1{*}10^{18}$	$4.63{*}10^{19}$
CB DOS	N_C $[cm^{-3}]$	$2.2{*}10^{18}$	$2.2{*}10^{18}$
VB DOS	N_V $[cm^{-3}]$	$1.8{*}10^{19}$	$5.0{*}10^{19}$
Mobility	μ_e, μ_h $[cm^2/Vs]$	100,100	1E-3,1E-3
Source	-	[81, 82]	[61, 96–98]

Atomic layer depositioned Nickel Oxide (ALD NiO) has often been reported as a potential candidate for the p-type material in the TRJ of perovskite/CIGS tandem cells [2, 32, 46]. ALD NiO is produced within the LAFLEX-2T project. The in-house electrical measurements resulted in E_g value of 3.82 eV, χ of 1.36 eV and a doping of 4.63 $*10^{19}$ cm^{-3} for the NiO material, see table 5.1 . The material exhibits interesting features: it is a p-type material, it has a high workfuction (ϕ = 5.2 eV)[1], and it has a high

[1]The in-house measured workfunction (ϕ) is 4.56 eV [61], although most literature on NiO stated values above 5.0 eV [96, 97]. This is more inline with the found doping concentration. The measuring of workfunction was done with *ultraviolet photoelectron spectroscopy* (UPS). UPS is found not to be reliable for determining ϕ, as the measurement creates charge inside the sample, which can lead to Fermi level shifting [99]

band offset for the conduction band in a junction with SnO_2. The features will be addressed in relation to the obtained band diagram (figure 5.1b).

The NiO electrical parameters were implemented and results can be seen in figures 5.1a and 5.1b. The effect of the higher doping of NiO becomes apparent when comparing figure 5.1a and 5.1b. In the baseline tandem stack with PEDOT:PSS, a misalignment is observed for $VB_{PEDOT:PSS}$ and CB_{SnO_2}. The introduction of NiO shows a VB_{NiO} situated close to the Fermi energy. This results in an alignment of the VB_{NiO} and CB_{SnO_2}. Due to the alignment efficient direct energy transport of charge carriers via B2BT becomes dominant (see figures 4.14a and 4.14b). Improving the transport in the TRJ leads to a better functioning tandem cell. This can be observed in figure 5.2 as it shows an improvement of external parameters in the J-V curve, similar to the previous observed trends in section 4.5. It even exceeds the highest found value of 12.84% PCE.

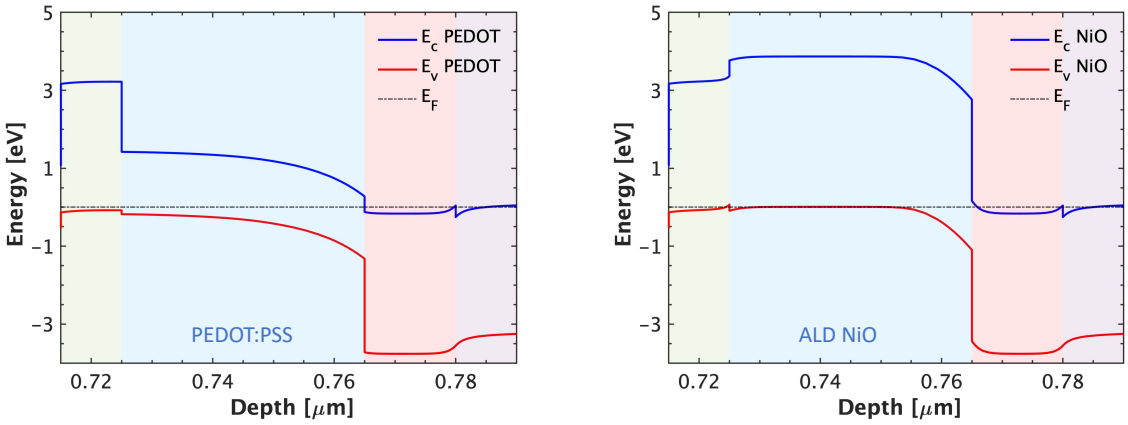

(a) The band diagram of the TRJ with PEDOT:PSS (blue area), SnO_2 (red area), and PTAA (green area)

(b) The band diagram of the TRJ with ALD NiO (blue area), SnO_2 (red area), and PTAA (green area)

Figure 5.1

Secondly, the implementation of NiO resulted in a higher band offset in the conduction band at the SnO_2 interface. Electrons move from the CIGS absorber layer towards the TRJ in SnO_2 and encounter the band offset at the interface. The larger barrier results in less thermionic emission. Thermionic emitted electrons will not contribute to recombination of non-collectable charge carrier in the TRJ, which is disadvantageous for the functioning of the cell. When thermionic emission is thus reduced, an improvement of the cell parameters is expected.

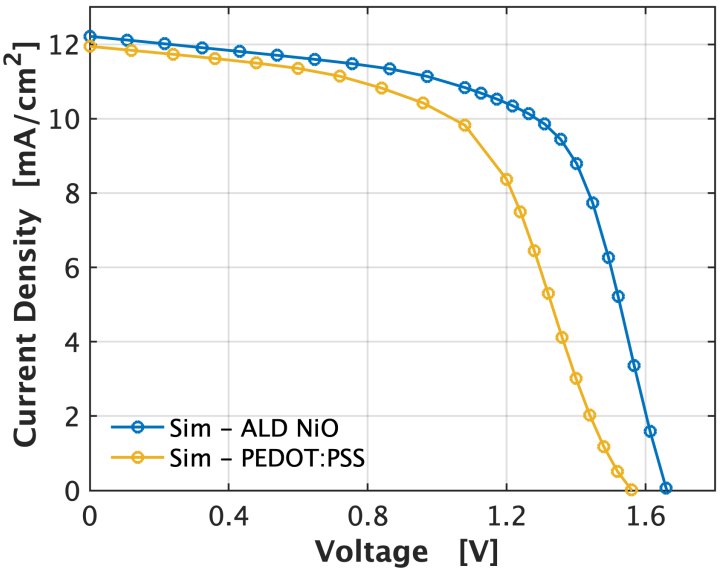

Figure 5.2: A comparison of the J-V curves for the tandem stack with PEDOT:PSS or ALD NiO

Table 5.2: A comparison of the external tandem cell parameters with PEDOT:PSS or NiO in the TRJ

External parameters	V_{oc} $[V]$	J_{sc} $[mA]$	FF	PCE [%]
PEDOT:PSS	1.567	11.94	56.90	10.63
ALD NiO	1.662	12.21	63.95	12.91

The introduction of NiO resulted in an improvement of 5.72% for the V_{OC} (1.567 V to 1.662 V) compared to the reference tandem cell. The FF improved from 56.90 to 63.95, which is +12.40%. The improvement of the J_{SC} is +2.26%. The J_{SC} is mostly dependant on light management and reduction of parasitic absorption and not so much on the transport mechanisms. NiO has higher bandgap than PEDOT:PSS and results in lower parasitic absorption [61]. The overall improvement of the PCE from 10.63% and 12.91% is observed. NiO was found to be an excellent candidate to substitute the PEDOT:PSS layer in the TRJ to improve the functioning of the perovskite/CIGS tandem cell.

5.2. Optical enhancement

In sections 4.4.3 and 4.4.4, the difference in generated current in both absorber layers was shown as well as the large reflectance losses that occur with the reference tandem stack. In this section we evaluate the performance by reducing the optical losses.

For current matching, the thickness of the perovskite layer was used as adjustable parameter as the CIGS bottom layer was obtained from a commercial party and cannot be altered. Figure 5.3 shows the result of the optimization. An optimal thickness for perovskite was found to be 312 nm. This reduction in perovskite thickness of 138 nm resulted in a decrease in top layer current (blue dotted arrow) but an increase in the CIGS absorbed photons (orange dotted arrow). This is due to less absorption of light in the 500 - 800 nm wavelength range in perovskite and an increase in absorption in CIGS. The trend of decreased absorption in the perovskite layer with reduced thickness can be expected, as the absorptance is depth dependant. Due to overlap in absorbance spectrum, as can be seen in figure 5.3, the photons will then be absorbed by the CIGS layer.

The result is an increase of 10.9% (+1.58 mA/cm^2) for the generated current in the limiting absorber layer and thus will result in an increase in the J_{SC} of the perovskite/CIGS tandem cell. The surface roughness of the bottom cell however limits the possible perovskite thickness, as a minimum of thickness is needed to fully cover the layer and not create any shunts. This thickness was found to be 300 nm minimal, meaning the current matching thickness exceeds this minimum layer thickness (312 nm > 300 nm).

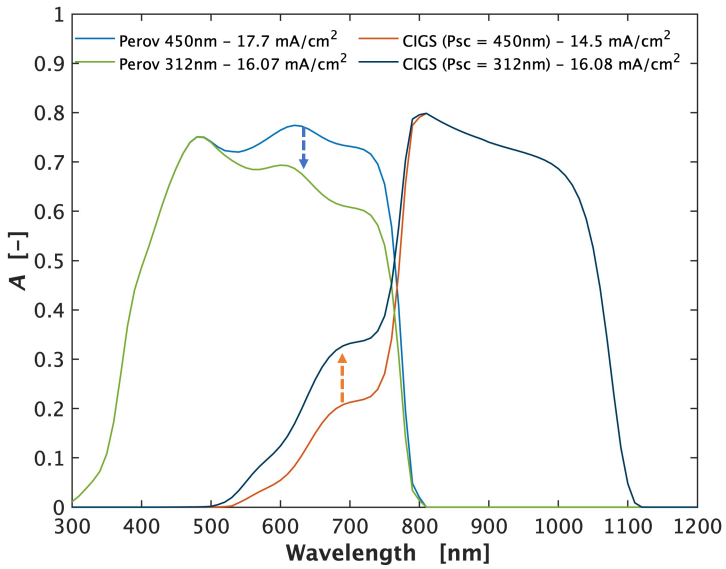

Figure 5.3: Optimization of the perovskite layer thickness resulting in current matching conditions for the perovksite/CIGS tandem cell. A value of 312 nm for the perovskite layer was found.

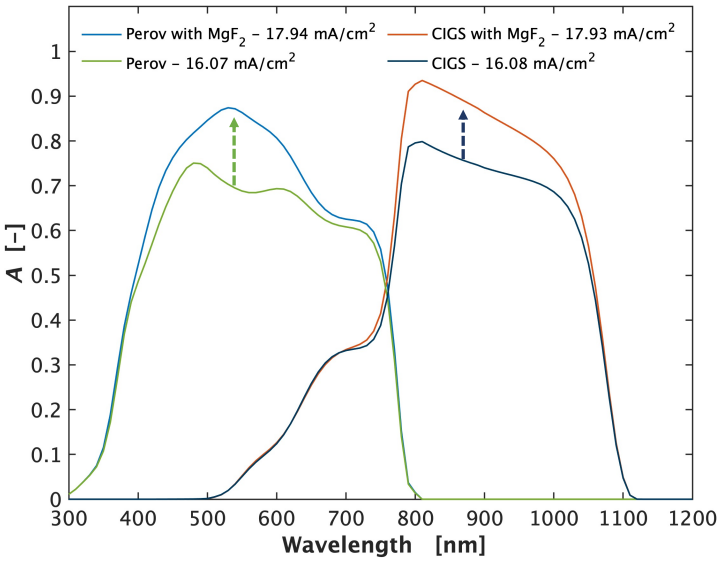

Figure 5.4: The effect of an anti-reflective coating added on top of the current matched baseline tandem. A 100 nm of MgF_2 was added.

Section 4.4.3 showed a 7.67 mA/cm^2 current loss due to reflection. To increase the absorbed light in the tandem, an anti-reflective coating (ARC) can be added. A top layer of MgF_2 of 100 nm was included on top of the baseline tandem layer stack. MgF_2 is a well documented, conventional ARC often used for lab-scale CIGS [22], and is suggested for minimizing optical losses in monolithic perovskite/c-Si tandem cells [60]. Also, the in-house produced perovskite cell used for the validation of the single-junction model has a MgF_2 layer. Figure 5.4 shows the effect of such an addition. The absorbed current in both absorber layers increases 11.57% which translates to 1.87 mA/cm^2. The increase in absorbed current can be seen from 400 nm to 1100 nm.

An overall optical improvement of 23% in the generated current density can be achieved (from 14.5 mA/cm^2 to 17.94 mA/cm^2) by reducing the thickness of perovskite to 312 nm and adding a 100 nm MgF_2 layer.

A second option to reach a current match in the tandem is by lowering the bandgap of CIGS to 1.0 eV. This can theoretically lead to a better current matching and higher yield in combination with the 1.6 eV bandgap value for perovskite [2]. Although an interesting insight, no more research was done on this matter as it was outside the scope of this thesis.

5.3. Carrier collection improvement

The band diagram of the single-junction Perovskite top cell in section 4.1 showed two band offsets, one at the PCBM/SnO_2 interface of 0.51 eV and one at the SnO_2/ITO interface (0.65 eV). This can be observed in the band diagram in figure 5.5. These band offset act as a barrier for the transport of the majority charge carriers when moving from the perovskite absorber layer towards the front contact. Also, a barrier potential inside the SnO_2 layer can be observed. This has effect on the external parameters.

Table 5.3: Varied parameters differences for the SnO_2 layer based research conducted by TU Eindhoven [6]

ALD temperature	T $[^\circ C]$	50	200
Electron affinity	χ $[eV]$	3.71	4.32
Bandgap	E_g $[eV]$	4.25	3.25
Carrier concentration	N_A $[*10^{19} cm^3]$	0.3	9.6
Mobility	μ $[cm^2/Vs]$	0.001	36

The used material is ALD SnO_2 at 50 $^\circ C$. The electrical parameters were found in Kuang et al. [6] and are summarised in table 5.3. The same research shows the possibility of tweaking the bandgap

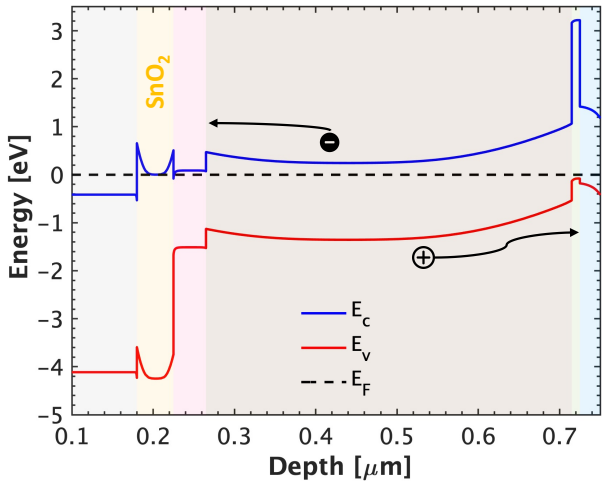

Figure 5.5: The top cell band diagram in the tandem cell. The carrier transport layer for electrons can be identified as the front SnO_2 (yellow), PCBM (pink) and ITO (light blue).

values from 4.25 to 3.25 eV and an increase of χ with 0.61 eV. To do this, the ALD temperature was increased to 200 $^{\circ}C$.

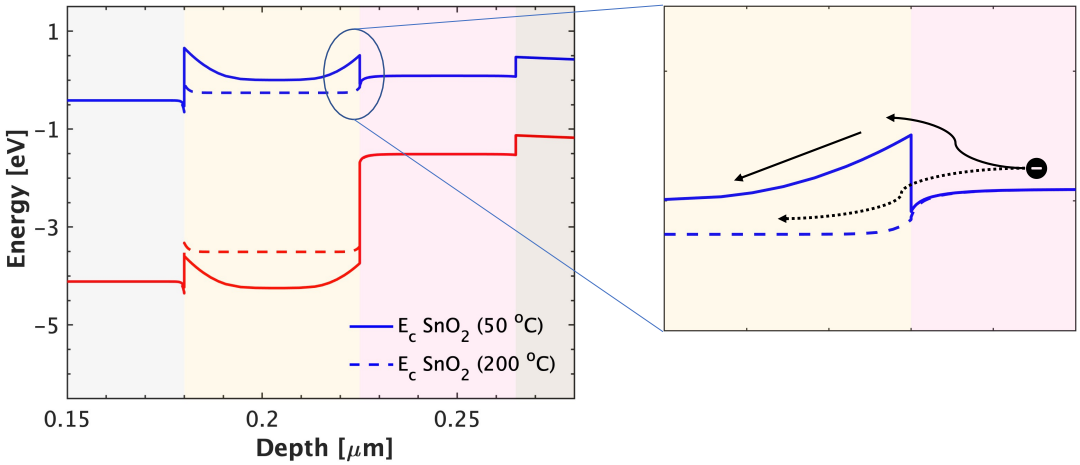

Figure 5.6: A zoom of the band diagram in in the SnO_2 layer (yellow) and PCBM layer (pink). Comparing the band offsets of ALD SnO_2 at 50 $^{\circ}C$ and 200 $^{\circ}C$.

Figure 5.6 shows the band diagram for implementation of the different SnO_2 materials. The band diagram shows that the band alignment for the ALD SnO_2 at 200$^{\circ}C$ does not create a band offset at the the SnO_2/PCBM interface (yellow and pink area). Also a reduction in the band offset at the ITO/SnO_2 interface is observed (from 0.65 to 0.17 eV). This can be contributed to the increased electron affinity as the CB is pushed down. In the band diagram for SnO_2 (50$^{\circ}C$) an potential barrier can be seen near the ITO/SnO_2 in the SnO_2 layer. This electric field acts as a barrier for electrons moving towards the front electrode. This barrier potential is significantly decreased for SnO_2 at 200 $^{\circ}C$.

The SnO_2 material has a second role: blocking holes from moving to the front side of the cell. The band diagram in figure 5.6 for the 200$^{\circ}C$ ALD SnO_2 still displays this attribute as the band offset of the valence band at the SnO_2/PCBM interface is still of significant height (2 eV) ensuring no hole transport towards the cathode electrode.

Figure 5.7 points out the effect of the better band alignment and reduction of the barrier potential on the external parameters. As expected, a better functioning cell was observed. The main change is seen in the J-V curve shape, indicating an improved FF from 66.08 to 75.33. This can be explained by the improved carrier transport of electrons, reducing the recombination in the absorber layer. This is inline with the observed results in Kuang et al. [6].

Although the results clearly indicate the beneficial effect of the depositing SnO_2 at 200 $^{\circ}C$, one has to

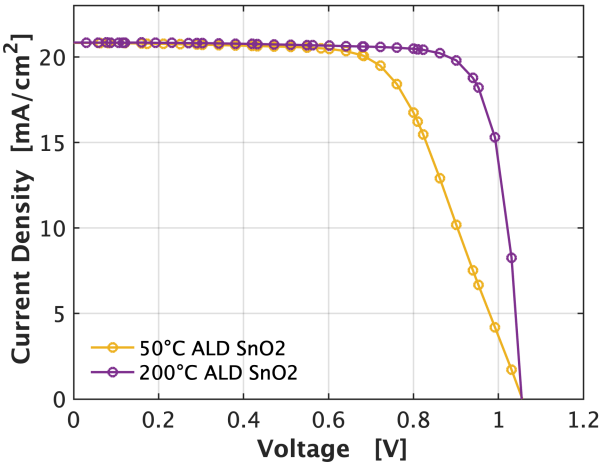

Figure 5.7: The J-V curve improvement by changing the ALD SnO_2 layer at 50 $^\circ C$ and 200 $^\circ C$ in the perovskite single-junction.

keep the production process of the tandem cell in mind. The top layer is deposited on the CIGS bottom layer, meaning the SnO_2 layer is deposited when the perovskite layer is already implemented. In real devices the temperature of processing could be detrimental for the final tandem, because decreases in device performance for perovskite solar cells have been observed for higher temperatures above 100 $^\circ C$ due to an increase in formation of defects and lowering of the bandgap [100]. The deposition temperature should therefore be kept below 100 $^\circ C$. Although Kuang et al. reports SnO_2 materials at ALD temperatures between 50 and 200 $^\circ C$, a significant increase in electron mobility is only reported at temperatures of 150 $^\circ C$ and higher. This deposition temperature would result in the degradation of the perovskite material.

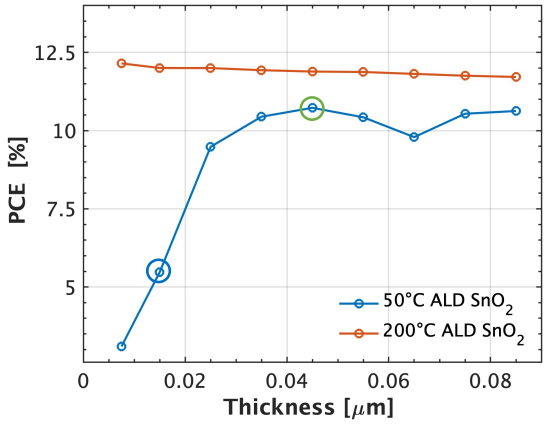

(a) The effect of thickness change in the SnO_2 layer on the efficiency of the tandem cell. For the circled points the band diagram is plotted in sub-figure 5.8b.

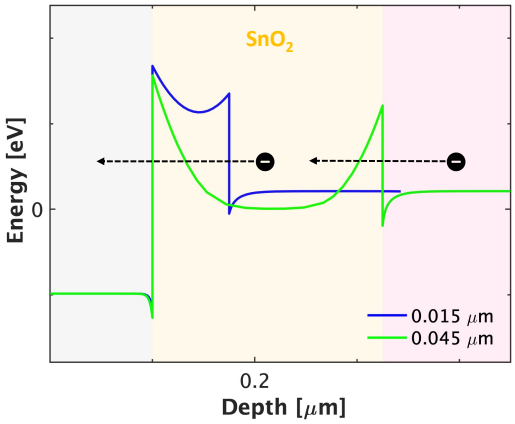

(b) The effect of SnO_2 on the band offsets around both interfaces in the tandem cell. The colors correspond to the efficiency figure 5.8a.

Figure 5.8

Figure 5.8a points out the effect of the thickness of the SnO_2 layer on the efficiency of the tandem cell by varying the thickness from 0.007 to 0.085 μm. For the 200 $^\circ C$ ALD, a small increasing trend is observed for thinner layer thicknesses (11.8% to 12.1%). When comparing 50 $^\circ C$ with 200 $^\circ C$ ALD, the effect of a better band alignment and decreased barrier potential is shown, as previously discussed. However, when reducing the thickness for the 50 $^\circ C$ ALD SnO_2, a decrease in PCE is seen for thicknesses below 0.035 μm, even resulting in a barely functioning cell for 0.015 μm.

This phenomenon can be explained by looking at figure 5.8b. For the indicated points in figure 5.8a, the CB band diagram was plotted. The two band offsets resulting in two barriers are observed at a thickness of 0.045 μm. The width of the barriers decreases with height. This increases the tunneling probability. Although there are two, the charge carriers can still transport through these heterojunctions by thermionic emission and direct tunneling resulting in a PCE of 10.7%.

As the thickness of SnO_2 is reduced, the two electric fields in the potential barriers are pushed towards each other. The two electric fields point in the opposite direction, and will cancel each other out. This results in a reduction of the barrier potential in the SnO_2 layer. This results in one thicker barrier (blue line) instead of two thinner ones (green line). This negatively affects the tunneling probability and results in a lower functioning tandem cell (PCE is 5.3%). We conclude that reducing the thickness of SnO_2 will not be beneficial for the solar cell.

Coincidentally, it was reported however, that a thin 0.015 μm layer of 50 $^{\circ}C$ ALD SnO_2 had no negative effect on the electron transport at the interfaces [6]. According to our modelling results, negative transport properties were found for 50 $^{\circ}C$ ALD SnO_2 . The conflicting results can be related to different cell configuration. The conclusion of the paper was based on a cell configuration without the addition of PCBM. The CB in figure 5.7 shows a drop of 0.45 eV in energy level when moving from perovskite to PCBM. The band offset at the SnO_2/PCBM interface was earlier discussed and equals 0.51 eV. When the perovskite layer is directly deposited on the SnO_2 layer, the band offset between perovskite and SnO_2 is potentially much smaller (0.06 eV) when compared to the band offset at SnO_2/PCBM interface. The reduction of the band offset at the SnO_2 interface reduces the limitation for electron transport. This can explain that no negative effect for the electron transport was found in Kuang et al.. The added PCBM layer for SnO_2 was however needed to prevent the degrading of the cell over time [6]. This addition of PCBM between SnO_2 and perovskite thus results in the two earlier discussed band offsets and barrier potential, worsening the carrier transport (figure 5.7).

The combination of the SnO_2 and PCBM is disadvantageous for the tandem cell, but the PCBM is needed to prevent the degration of the PCE when using SnO_2. Secondly, the band alignment of PCBM with ITO and perovskite shows very promising characteristics for electron transport towards the cathode electrode without SnO_2, see figure 5.5. This reasoning suggests that a possible adjustment would be to leave the SnO_2 out of the tandem layer stack and use PCBM as the only ETL connection to the ITO [101] and should be studied in future work.

5.4. Recombination reduction

The main recombination mechanism in the top cell was identified in section 4.4.4 as SRH, mostly facilitated by the defects present in the perovskite absorber layer and accounted for 3.889 mA/cm^2 in SC condition. A possible solution for this loss is the passivation of the trap states. Passivation of traps has resulted in the successful enhancement of obtained efficiencies in perovskite single-junction solar cells [94, 102, 103]. To research the effect of passivation, the single-junction perovskite model was run with a reduction of the trap state density for the HTL (PTAA/perovskite interface), the ETL (perovskite/PCBM interface), and the bulk. The simulation results are presented in figure 5.9. The reduction in the ETL and bulk gave similar results as the tandem cell with baseline trap distribution described in chapter 3 and show no significant difference in the J-V curve. For the passivation of the traps at the HTL, an increase in the V_{OC} is observed of 0.081 V.

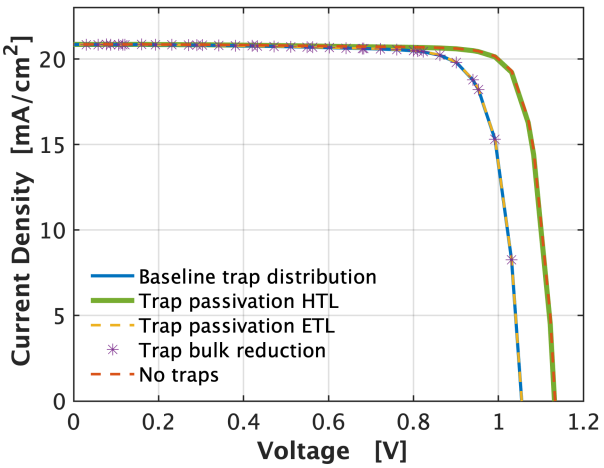

Figure 5.9: Effect of trap passivation on J-V curve in the perovskite single-junction. The trap concentration was reduced to $1*10^2$ cm^{-3} for the bulk, HTL and ETL.

The effect of HTL passivation on the V_{OC} can be related to the higher defect concentration that was modelled at the PTAA/perovskite interface. Higher trap state concentration directly translates to a higher amount of recombination centers. As the recombination rate has a direct influence on the V_{OC} and the PCE, reducing the concentration is reflected in the J-V curve. Secondly, at the HTL, the mid bandgap trap states are situated closer to the Fermi level (see figure 5.5, right side of perovskite) than at the ETL (see figure 5.5, left side of perovskite) due to band bending, resulting in more active recombination centers contributing to the recombination process. As the capture rate of charge carriers is driven by the Fermi energy level relative to the trap state distribution, at the HTL more trap states are able to contribute to the recombination process. When reducing the active trap states via passiviation techniques, an improvement of the cell performance is observed.

5.5. Efficiency optimization

This section aims to investigate the possible improvements that can be done to the baseline perovskite/CIGS tandem that was introduced in the first chapter of this thesis. The following improvements were based on the loss analysis and transport analysis of the baseline tandem cell in chapter 4. We have four propositions for the improvement the cell: 1) Improving carrier transport by implementing NiO as the p-type layer in the TRJ, 2) Optical enhancement of the cell by reducing the perovskite thickness and adding a MgF_2 ARC, 3) Improving the carrier transport in the top cell the by changing the front SnO_2 at 50 $^{\circ}C$ to SnO_2 at 200 $^{\circ}C$. 4) Reduce SRH recombination in the perovskite layer by defect passivation.

Proposition 1: substitute PEDOT:PSS with ALD NiO as the p-type material in the TRJ. This proposition is related to results found in the analysis of the tunnel recombination junction. The PEDOT:PSS material was limiting the charge carrier transport thanks to its electrical parameters that resulted in a sub-optimal band alignment of the CB in the middle Tin Oxide (m SnO_2) and the VB of PSS:PEDOT. The electrical parameters of Nickel Oxide (NiO) resulted in the band alignment of VB_{NiO} and CB_{SnO_2} and a higher band offset at the SnO_2-interface. The NiO was implemented in the baseline tandem stack and the PCE increased from 10.63 to 12.91% (figure 5.10).

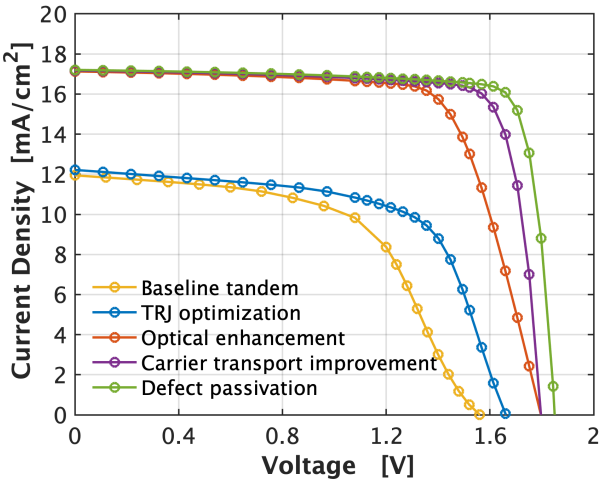

Figure 5.10: The effect of the optimization techniques on the baseline tandem J-V curve.

Proposition 2: reduce the thickness of the perovskite absorber layer and add an ARC on top of the tandem layer stack. The loss analysis showed the limiting current of CIGS on the total tandem. By reducing the perovskite layer thickness to 312 nm, a current match between top and bottom layer is achieved, increasing the current density in CIGS from 14.5 to 16.08 mA/cm^2 while remaining above the minimal of 300 nm thickness to prevent shunting. As the reflectance losses were found to be significant, a Magnesium Fluoride (MgF_2) ARC was added, increasing the current density created by photon absorption from 16.07 to 17.70 mA/cm^2. Figure 5.10 shows effect of the implementation of the optical improvements on the tandem cell. The eventual J_{SC} is increased from 12.21 mA/cm^2 to 17.21

mA/cm^2. The value is lower than the earlier mentioned 17.70 mA/cm^2 due to metalisation losses. An increase in V_{OC} is observed from 1.662 to 1.802 V. This results in a significant increase in the functioning of the tandem cell (blue line vs. red line, figure 5.10)

Proposition 3: alter the front SnO_2 by using 200 $^\circ C$ ALD SnO_2 instead of 50 $^\circ C$ ALD SnO_2. Due to its smaller bandgap and larger electron affinity, a better band alignment with ITO and PCBM and smaller barrier potential is formed. This results in better transport of charge carriers to the front electrode. Consequently, a higher efficiency for the tandem cell (10.7 to 11.9%) and better FF for the top cell is observed. Figure 5.10 shows the effect of the improved charge carrier transport on the FF of the tandem cell (red vs. purple line). The FF is improved from 66.30 to 83.87 in the tandem cell after the substitution of 50 $^\circ C$ ALD SnO_2 with 200 $^\circ C$ ALD SnO_2.

Proposition 4: reduce the defects in the perovskite absorber layer by defect passivation. The non-radiative SRH recombination in the perovskite layer was found to the dominant loss mechanism in the absorber layer. The defects at the PTAA/perovskite interface were found to be most limiting in the functioning of the cell due to high concentration of trap states ($1*10^{17}\ cm^{-3}$). The reduction of traps in the absorber layer resulted in an increase in the V_{OC} in the single-junction. The results for the tandem cell are observed in figure 5.10. A V_{OC} increase from 1.802 V to 1.849 V is seen (purple vs. green line).

The step-wise implementation of the four propositions resulted in an improvement of the external parameters of the perovskite/CIGS tandem cell compared to the reference tandem, see table 5.4. The overall increase of the efficiency is 16.1 percentage points: 10.7 to 26.8%. This exceeds the minimum efficiency goal of the LAFLEX-2T project of 19.0%. All improvements were related to the perovskite top cell layer stack, meaning the implementation could be achievable without the need of modification of the CIGS layer stack. The 26.8 % is comparable to the highest found values for modelling results of perovskite/CIGS tandem solar cells (table 1.1) and is nearing the maximum obtainable efficiency for 2T perovskite/CIGS tandem cells of 32.0 % [2].

Table 5.4: The final comparison of the baseline tandem with the optimized perovskite/CIGS cell.

External parameters	V_{oc} $[V]$	J_{sc} $[mA]$	FF	PCE [%]
Baseline Tandem	1.567	11.94	56.90	10.63
Optimized Tandem	1.849	17.21	83.87	26.69

6
Conclusion

An optical and electrical loss analysis of a perovskite/CIGS tandem cell was presented in this thesis. Through GENPRO4 optical simulations, the charge carrier generation profile for each layer was obtained. TCAD Sentaurus modelling software was used for the electrical simulation, which solves the fundamental semiconductor physics equations. With the electrical parameters of each layer as input, the current losses and transport limiting layers could be identified. These insights can be used to improve the existing layer stack and thereby enhancing the functioning of the solar cell. In this chapter, we conclude this research by looking back at the thesis objectives.

Objective 1: Develop a realistic modelling template for the perovskite/CIGS baseline tandem cell

In chapter 3, an opto-electrical model for the perovskite/CIGS baseline tandem cell was presented, and successfully validated in chapter 4 using experimentally obtained data for the J-V curve. The overall approach made use of two separate models of a single-junction perovskite cell and a single-junction CIGS cell, which first were validated using experimentally obtained data. For both models, trap state distributions were added in the absorber layers, which could potentially facilitate the recombination of charge carriers. The J-V curve results from the models were both in good agreement with experimental J-V curve data of both single junctions. The electrical parameters from the materials in both models were implemented in a tandem model with the perovskite as the top cell and CIGS as the bottom cell. In the tandem model, the dependency on direct and indirect energy carrier transport in the tunnel recombination junction became apparent. For direct energy transport of the charge carriers, the band to band tunneling (B2BT) mechanism was used. For the indirect energy transport, trap assisted tunneling (TAT) was successfully implemented using the non-local local TAT model facilitated by trap states in mid bandgap of PEDOT:PSS following a Gaussian energy distribution. The tandem model was validated using experimental J-V curve data. The model was able to reasonably reproduce experimental J-V curves. It can thus accurately reproduce the physical mechanisms in the baseline tandem cell. This model was used for the next objective.

Objective 2: Perform an optical and electrical loss analysis of the baseline tandem cell

Chapter 4 presented an extensive analysis of the losses in the baseline perovskite/CIGS tandem cell and analysed the transport of charge carriers through the TRJ. First, a breakdown of the incoming photo-current (J_{ph} = 46.45 mA/cm^2) was obtained from the electrical model. This showed that, due to parasitic absorption, 5.32 mA/cm^2 is lost. The Molybdenum (Mo) back-contact was identified as the main contributor to the parasitic losses and was responsible for a loss of 2.01 mA/cm^2. Reflectance losses are responsible for losing 23.5% of the incoming current in the tandem cell (10.92 mA/cm^2). The breakdown of the photo-current also revealed the current mismatch between the top and bottom layer of the tandem cell (16.67 mA/cm^2 vs. 13.54 mA/cm^2 for the top and bottom cell, respectively). The recombination losses in the top and bottom cells were extracted, showing the non-radiative recombination processes related to defects in the material as the dominant recombination mechanism in both absorber layers. This includes Shockley-Read-Hall and the surface recombination. The losses in the top cell when operating at short circuit (SC) conditions were 4.71 mA/cm^2. For the bottom cell, the losses were equal to 1.59 mA/cm^2. The non-radiative losses in SC conditions were attributed to the defect states in the absorber materials. The recombination losses in the top and bottom cell at SC conditions were also compared to the recombination losses at maximum power point (MPP). The increase in recombination losses of 2.12 mA/cm^2 was attributed to limited transport of charge carriers towards the electrodes resulting in a low fill factor (FF).

An extensive analysis of carrier transport through the TRJ revealed the dependency on in-direct energy transport of charge carriers in the baseline tandem cell. This indicated that the charge carrier transport was dominated by the TAT mechanism. The modelling of the TRJ for different dopings of the p-type and n-type material showed that optimal values for the external solar cell parameters were found for band alignment of the $VB_{PEDOT:PSS}$ and CB_{SnO_2}. Due alignment of the bands, direct energy transport of carriers is possible. This resulted in the more efficient B2BT mechanism becoming dominant. It was concluded that for the baseline tandem cell, an improvement in the p-type region could be made by reducing the energy difference between the VB and the Fermi level, resulting in band alignment in the TRJ.

Objective 3: Propose recommendations and guidelines for the optimization of the baseline tandem cell

Chapter 5 used the insights from chapter 4 to come up with four propositions to improve the functioning of the baseline tandem cell: 1) Substitute PEDOT:PSS in the TRJ with ALD NiO. Due NiO's electrical parameters an improved band alignment of the VB_{p-type} with the CB_{SnO_2} was observed, resulting in an increase in PCE from 10.63% to 12.91%. 2) Reduce the thickness of the perovskite absorber layer to 312 nm and add a 100 nm MgF_2 ARC on top of the layer stack. This resulted in an increase of the J_{SC} from 12.21 mA/cm^2 to 17.21 mA/cm^2 due to current matching of the top and bottom cell and the improved trapping of the incoming light. 3) Change the material for the front SnO_2 from 50 $^\circ C$ ALD SnO_2 to 200 $^\circ C$ ALD SnO_2. This will improve charge transport to the front electrode as limiting band offsets at the interfaces of the SnO_2 and barrier potential in the SnO_2 layer are reduced, resulting in a higher FF (66.30 to 83.87). 4) Reduce the defects in the perovskite absorber layer by defect passivation. This will reduce the SRH and surface recombination in the perovskite top cell, improving the V_{OC} from 1.80 V to 1.849 V. We conclude that a PCE of 26.69% is obtainable for the baseline perovskite/CIGS tandem cell when implementing the four propositions, see figure 6.1.

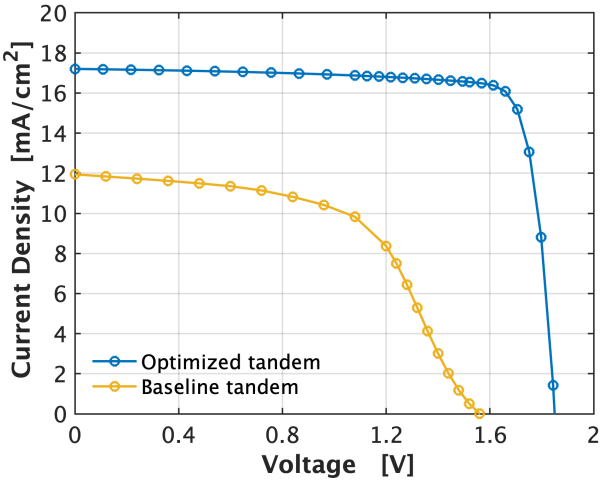

Figure 6.1: The J-V curve of the final optimized perovskite/CIGS tandem cell with 26.69%.

Bibliography

[1] T. Todorov, O. Gunawan, and S. Guha, *A road towards 25% efficiency and beyond: Perovskite tandem solar cells,* Molecular Systems Design and Engineering **1**, 370 (2016).

[2] T. J. Jacobsson, A. Hultqvist, S. Svanström, L. Riekehr, U. B. Cappel, E. Unger, H. Rensmo, E. M. Johansson, M. Edoff, and G. Boschloo, *2-Terminal CIGS-perovskite tandem cells: A layer by layer exploration,* Solar Energy **207**, 270 (2020).

[3] D. A. Neamen, B. Burr, R. Ll, D. La Mad~son, W. New, Y. San, F. St, L. B. Bogota, C. Kualalurnpur, L. London, M. Mex~coclty, M. Montreal, N. Sant~ago, S. Singapore, and S. T. Toronto, *Semiconductor Physics and Devices Basic Principles Third Edition*, Tech. Rep. (2003).

[4] Inc. Synopsys., *Sentaurus Device User Guide version K-2015.06,* (2015).

[5] Z. Ni, S. Xu, and J. Huang, *Resolving spatial and energetic distributions of trap states in metal halide perovskite solar cells,* Science **371**, 1352 (2021).

[6] Y. Kuang, V. Zardetto, R. Van Gils, S. Karwal, D. Koushik, M. A. Verheijen, L. E. Black, C. Weijtens, S. Veenstra, R. Andriessen, W. M. Kessels, and M. Creatore, *Low-Temperature Plasma-Assisted Atomic-Layer-Deposited SnO2 as an Electron Transport Layer in Planar Perovskite Solar Cells,* ACS Applied Materials and Interfaces **10**, 30367 (2018).

[7] M. E. Eberhart, *Feeding the fire: The lost history and uncertain future of mankind's energy addiction,* , 14 (2007).

[8] M. Victoria, N. Haegel, I. M. Peters, R. Sinton, A. Jäger-Waldau, C. del Cañizo, C. Breyer, M. Stocks, A. Blakers, I. Kaizuka, K. Komoto, and A. Smets, *Solar photovoltaics is ready to power a sustainable future,* Joule (2021), 10.1016/j.joule.2021.03.005.

[9] International Renewable Energy Agency, *WORLD ENERGY TRANSITIONS OUTLOOK 1.5° C PATHWAY* (2021).

[10] International Renewable Energy Agency, *Renewable power generation costs in 2019* (2020).

[11] D. M. Chapin, C. S. Fuller, and G. L. Pearson, *A new silicon p-n junction photocell for converting solar radiation into electrical power,* (1954).

[12] A. Smets, *Solar energy: The physics and engineering of photovoltaic conversion, technologies and systems*, Vol. 1 (2015).

[13] A. Kojima, K. Teshima, Y. Shirai, and T. Miyasaka, *Organometal halide perovskites as visible-light sensitizers for photovoltaic cells,* Journal of the American Chemical Society **131**, 6050 (2009).

[14] W. Shockley and H. J. Queisser, *Detailed balance limit of efficiency of p-n junction solar cells,* Journal of Applied Physics **32**, 510 (1961).

[15] F. Fu, T. Feurer, T. P. Weiss, S. Pisoni, E. Avancini, C. Andres, S. Buecheler, and A. N. Tiwari, *High-efficiency inverted semi-transparent planar perovskite solar cells in substrate configuration,* Nature Energy **2**, 16190 (2017).

[16] H. Li and W. Zhang, *Perovskite Tandem Solar Cells: From Fundamentals to Commercial Deployment, Chemical Reviews*, **120**, 9835 (2020).

[17] G. Han, S. Zhang, P. P. Boix, L. H. Wong, L. Sun, and S. Y. Lien, *Towards high efficiency thin film solar cells, Progress in Materials Science*, **87**, 246 (2017).

[18] M. Mousa, M. M. Salah, F. Z. Amer, A. Saeed, and R. I. Mubarak, *High Efficiency Tandem Perovskite/CIGS Solar Cell,* Institute of Electrical and Electronics Engineers Inc. **7**, 6050 (2020).

[19] *Maximizing tandem solar cell power extraction using a three-terminal design,* Sustainable Energy and Fuels **2**, 1141 (2018).

[20] S. R. Kodigala, *Cu(In1-xGax)Se2 Based Thin Film Solar Cells* (Academic Press, 2010) p. 700.

[21] S. Minoura, T. Maekawa, K. Kodera, A. Nakane, S. Niki, and H. Fujiwara, *Optical constants of Cu(In, Ga)Se2 for arbitrary Cu and Ga compositions,* Journal of Applied Physics **117** (2015), 10.1063/1.4921300.

[22] N. Rezaei, *Opto-electrical Modelling of CIGS Solar Cells* (2019).

[23] M. A. Green, A. Ho-Baillie, and H. J. Snaith, *The emergence of perovskite solar cells,* (2014).

[24] F. Bella, P. Renzi, C. Cavallo, and C. Gerbaldi, *Caesium for Perovskite Solar Cells: An Overview,* (2018).

[25] T. Jesper Jacobsson, J. P. Correa-Baena, M. Pazoki, M. Saliba, K. Schenk, M. Grätzel, and A. Hagfeldt, *Exploration of the compositional space for mixed lead halogen perovskites for high efficiency solar cells,* Energy and Environmental Science **9**, 1706 (2016).

[26] E. L. Unger, E. T. Hoke, C. D. Bailie, W. H. Nguyen, A. R. Bowring, T. Heumüller, M. G. Christoforo, and M. D. McGehee, *Hysteresis and transient behavior in current-voltage measurements of hybrid-perovskite absorber solar cells,* Energy and Environmental Science **7**, 3690 (2014).

[27] W. Tress, N. Marinova, T. Moehl, S. M. Zakeeruddin, M. K. Nazeeruddin, and M. Grätzel, *Understanding the rate-dependent J-V hysteresis, slow time component, and aging in CH3NH3PbI3 perovskite solar cells: The role of a compensated electric field,* Energy and Environmental Science **8**, 995 (2015).

[28] R. V. Heerden, *Slow sub-gap energy states as the origin of hysteresis in perovskite solar cells,* (2020).

[29] Y. Yang Michael, Q. Chen, Y. T. Hsieh, T. B. Song, N. D. Marco, H. Zhou, and Y. Yang, *Multilayer Transparent Top Electrode for Solution Processed Perovskite/Cu(In,Ga)(Se,S)2 Four Terminal Tandem Solar Cells,* ACS Nano **9**, 7714 (2015).

[30] *Semi-transparent perovskite solar cells for tandems with silicon and CIGS,* Energy and Environmental Science **8**, 956 (2015).

[31] Q. Han, Y. T. Hsieh, L. Meng, J. L. Wu, P. Sun, E. P. Yao, S. Y. Chang, S. H. Bae, T. Kato, V. Bermudez, and Y. Yang, *High-performance perovskite/ Cu(In,Ga)Se2 monolithic tandem solar cells,* Science **361**, 904 (2018).

[32] M. Jošt, T. Bertram, D. Koushik, J. A. Marquez, M. A. Verheijen, M. D. Heinemann, E. Köhnen, A. Al-Ashouri, S. Braunger, F. Lang, B. Rech, T. Unold, M. Creatore, I. Lauermann, C. A. Kaufmann, R. Schlatmann, and S. Albrecht, *21.6%-Efficient Monolithic Perovskite/Cu(In,Ga)Se 2 Tandem Solar Cells with Thin Conformal Hole Transport Layers for Integration on Rough Bottom Cell Surfaces,* ACS Energy Letters **4**, 583 (2019).

[33] A. Kumar, S. D. Saurabh, and H. Sharma, *Perovskite-CIGS materials based tandem solar cell with an increased efficiency of 27.5%,* Materials Today: Proceedings (2021), 10.1016/j.matpr.2021.01.565.

[34] T. Todorov, T. Gershon, O. Gunawan, Y. S. Lee, C. Sturdevant, L. Y. Chang, and S. Guha, *Monolithic Perovskite-CIGS Tandem Solar Cells via in Situ Band Gap Engineering,* Advanced Energy Materials **5** (2015), 10.1002/aenm.201500799.

[35] M. Nakamura, K. Tada, T. Kinoshita, T. Bessho, C. Nishiyama, I. Takenaka, Y. Kimoto, Y. Higashino, H. Sugimoto, and H. Segawa, *Perovskite/CIGS Spectral Splitting Double Junction Solar Cell with 28% Power Conversion Efficiency,* iScience **23**, 101817 (2020).

[36] D. H. Kim, C. P. Muzzillo, J. Tong, A. F. Palmstrom, B. W. Larson, C. Choi, S. P. Harvey, S. Glynn, J. B. Whitaker, F. Zhang, Z. Li, H. Lu, M. F. van Hest, J. J. Berry, L. M. Mansfield, Y. Huang, Y. Yan, and K. Zhu, *Bimolecular Additives Improve Wide-Band-Gap Perovskites for Efficient Tandem Solar Cells with CIGS,* Joule **3**, 1734 (2019).

[37] H. Shen, T. Duong, J. Peng, D. Jacobs, N. Wu, J. Gong, Y. Wu, S. K. Karuturi, X. Fu, K. Weber, X. Xiao, T. P. White, and K. Catchpole, *Mechanically-stacked perovskite/CIGS tandem solar cells with efficiency of 23.9% and reduced oxygen sensitivity,* Energy and Environmental Science **11**, 394 (2018).

[38] A. Guchhait, H. A. Dewi, S. W. Leow, H. Wang, G. Han, F. B. Suhaimi, S. Mhaisalkar, L. H. Wong, and N. Mathews, *Over 20% Efficient CIGS-Perovskite Tandem Solar Cells,* ACS Energy Letters **2**, 807 (2017).

[39] U. W. Paetzold, M. Jaysankar, R. Gehlhaar, E. Ahlswede, S. Paetel, W. Qiu, J. Bastos, L. Rakocevic, B. S. Richards, T. Aernouts, M. Powalla, and J. Poortmans, *Scalable perovskite/CIGS thin-film solar module with power conversion efficiency of 17.8%,* Journal of Materials Chemistry A **5**, 9897 (2017).

[40] C. Xu, Z. Liu, and E. C. Lee, *High-performance metal oxide-free inverted perovskite solar cells using poly(bis(4-phenyl)(2,4,6-trimethylphenyl)amine) as the hole transport layer,* Journal of Materials Chemistry C **6**, 6975 (2018).

[41] M. B. Islam, M. Yanagida, Y. Shirai, Y. Nabetani, and K. Miyano, *NiOx Hole Transport Layer for Perovskite Solar Cells with Improved Stability and Reproducibility,* ACS Omega **2**, 2291 (2017).

[42] J. Ciro, D. Ramírez, M. A. Mejía Escobar, J. F. Montoya, S. Mesa, R. Betancur, and F. Jaramillo, *Self-Functionalization behind a Solution-Processed NiOx Film Used As Hole Transporting Layer for Efficient Perovskite Solar Cells,* ACS Applied Materials and Interfaces **9**, 12348 (2017).

[43] G. Li, Y. Jiang, S. Deng, A. Tam, P. Xu, M. Wong, and H. S. Kwok, *Overcoming the Limitations of Sputtered Nickel Oxide for High-Efficiency and Large-Area Perovskite Solar Cells,* Advanced Science **4**, 1700463 (2017).

[44] K. A. Bush, S. Manzoor, K. Frohna, Z. J. Yu, J. A. Raiford, A. F. Palmstrom, H. P. Wang, R. Prasanna, S. F. Bent, Z. C. Holman, and M. D. McGehee, *Minimizing Current and Voltage Losses to Reach 25% Efficient Monolithic Two-Terminal Perovskite-Silicon Tandem Solar Cells,* ACS Energy Letters **3**, 2173 (2018).

[45] F. A. Rubinelli, J. K. Rath, and R. E. Schropp, *Microcrystalline n-i-p tunnel junction in a-Si:H/a-Si:H tandem cells,* Journal of Applied Physics **89**, 4010 (2001).

[46] M. De Bastiani, A. S. Subbiah, E. Aydin, F. H. Isikgor, T. G. Allen, and S. De Wolf, *Recombination junctions for efficient monolithic perovskite-based tandem solar cells: Physical principles, properties, processing and prospects,* Materials Horizons **7**, 2791 (2020).

[47] M. Filipic, P. Loper, B. Niesen, S. De Wolf, J. Krc, C. Ballif, and M. Topic, *CH3NH3PbI3 perovskite silicon tandem solar cells: characterization based optical simulations,* Optics Express **23**, A263 (2015).

[48] H. Q. Tan, X. Zhao, E. Birgersson, F. Lin, and H. Xue, *Optoelectronic modeling and sensitivity analysis of a four-terminal all-perovskite tandem solar cell – Identifying pathways to improve efficiency,* Solar Energy **216**, 589 (2021).

[49] Q. Zhao, R. Wu, Z. Zhang, J. Xiong, Z. He, B. Fan, Z. Dai, B. Yang, X. Xue, P. Cai, S. Zhan, X. Zhang, and J. Zhang, *Achieving efficient inverted planar perovskite solar cells with nondoped PTAA as a hole transport layer,* Organic Electronics **71**, 106 (2019).

[50] U. Aeberhard, R. Hausermann, A. Schiller, B. Blulle, and B. Ruhstaller, *Analysis and optimization of perovskite-silicon tandem solar cells by full opto-electronic simulation, Proceedings of the International Conference on Numerical Simulation of Optoelectronic Devices, NUSOD,* **1**, 37 (2020).

[51] R. Santbergen, A. H. Smets, and M. Zeman, *Optical model for multilayer structures with coherent, partly coherent and incoherent layers,* Optics Express, Vol. 21, Issue S2, pp. A262-A267 **21**, A262 (2013).

[52] F. Jiménez-Molinos, F. Gámiz, A. Palma, P. Cartujo, and J. A. López-Villanueva, *Direct and trap-assisted elastic tunneling through ultrathin gate oxides,* Journal of Applied Physics **91**, 5116 (2002).

[53] R. A. Vijayan, S. Essig, S. De Wolf, B. G. Ramanathan, P. Loper, C. Ballif, and M. Varadharajaperumal, *Hole-Collection Mechanism in Passivating Metal-Oxide Contacts on Si Solar Cells: Insights from Numerical Simulations,* IEEE Journal of Photovoltaics **8**, 473 (2018).

[54] J. C. Ranuárez, M. J. Deen, and C. H. Chen, *A review of gate tunneling current in MOS devices,* Microelectronics Reliability **46**, 1939 (2006).

[55] E. Merzbacher, J. Wiley, N. York, . Chichester, . Weinheim, and B. . Singapore, *Ouantum Mechanics THIRD EDITION* (1961).

[56] M. K. Ieong, P. M. Solomon, S. E. Laux, H. S. P. Wong, and D. Chidambarrao, *Comparison of raised and Schottky source/drain MOSFETs using a novel tunneling contact model,* Technical Digest - International Electron Devices Meeting , 733 (1998).

[57] F. Smole and J. Furlan, *Effects of abrupt and graded a-Si:C:H/a-Si:H interface on internal properties and external characteristics of p-i-n a-Si:H solar cells,* Journal of Applied Physics **72**, 5964 (1992).

[58] A. Gehring and S. Selberherr, *Modeling of tunneling current and gate dielectric reliability for nonvolatile memory devices,* IEEE Transactions on Device and Materials Reliability **4**, 306 (2004).

[59] C. Messmer, M. Bivour, J. Schon, S. W. Glunz, and M. Hermle, *Numerical Simulation of Silicon Heterojunction Solar Cells Featuring Metal Oxides as Carrier-Selective Contacts,* IEEE Journal of Photovoltaics **8**, 456 (2018).

[60] R. Santbergen, R. Mishima, T. Meguro, M. Hino, H. Uzu, J. Blanker, K. Yamamoto, and M. Zeman, *Minimizing optical losses in monolithic perovskite/c-Si tandem solar cells with a flat top cell,* Optics Express, Vol. 24, Issue 18, pp. A1288-A1299 **24**, A1288 (2016).

[61] TNO, *Inhouse measurements performed within the LAFLEX2T,* (2021).

[62] R. Santbergen, T. Meguro, T. Suezaki, G. Koizumi, K. Yamamoto, and M. Zeman, *GenPro4 Optical Model for Solar Cell Simulation and Its Application to Multijunction Solar Cells,* IEEE Journal of Photovoltaics **7**, 919 (2017).

[63] A. A. Al-Shouq and A. B. Gougam, *Review of interdigitated back contacted full heterojunction solar cell (IBC-SHJ): A simulation approach,* 3D Stacked Chips: From Emerging Processes to Heterogeneous Systems , 309 (2016).

[64] C. Canali, G. Majni, R. Minder, and G. Ottaviani, *Electron and Hole Drift Velocity Measurements in Silicon and Their Empirical Relation to Electric Field and Temperature,* IEEE Transactions on Electron Devices **22**, 1045 (1975).

[65] D. J. Roulston, N. D. Arora, and S. G. Chamberlain, *Modeling and Measurement of Minority-Carrier Lifetime versus Doping in Diffused Layers of n +-p Silicon Diodes,* IEEE Transactions on Electron Devices **29**, 284 (1982).

[66] C. Frisk, C. Platzer-Björkman, J. Olsson, P. Szaniawski, J. T. Wätjen, V. Fjällström, P. Salomé, and M. Edoff, *Optimizing Ga-profiles for highly efficient Cu(In, Ga)Se2 thin film solar cells in simple and complex defect models,* Journal of Physics D: Applied Physics **47**, 485104 (2014).

[67] J. Yuan, L. Zhang, C. Bi, M. Wang, and J. Tian, *Surface Trap States Passivation for High-Performance Inorganic Perovskite Solar Cells,* Solar RRL **2**, 1800188 (2018).

[68] A. A. Mamun, T. T. Ava, K. Zhang, H. Baumgart, and G. Namkoong, *New PCBM/carbon based electron transport layer for perovskite solar cells,* Physical Chemistry Chemical Physics **19**, 17960 (2017).

[69] A. Schenk, *A model for the field and temperature dependence of Shockley-Read-Hall lifetimes in silicon,* Solid-State Electronics **35**, 1585 (1992).

[70] G. A. Hurkx, D. B. Klaassen, and M. P. Knuvers, *A New Recombination Model for Device Simulation Including Tunneling,* IEEE Transactions on Electron Devices **39**, 331 (1992).

[71] P. Procel, H. Xu, A. Saez, C. Ruiz-Tobon, L. Mazzarella, Y. Zhao, C. Han, G. Yang, M. Zeman, and O. Isabella, *The role of heterointerfaces and subgap energy states on transport mechanisms in silicon heterojunction solar cells,* Progress in Photovoltaics: Research and Applications **28**, 935 (2020).

[72] A. Palma, A. Godoy, J. A. Jiménez-Tejada, J. E. Carceller, and J. A. López-Villanueva, *Quantum two-dimensional calculation of time constants of random telegraph signals in metal-oxide–semiconductor structures,* Physical Review B **56**, 9565 (1997).

[73] E. Aydin, M. D. Bastiani, X. Yang, M. Sajjad, F. Aljamaan, Y. Smirnov, M. N. Hedhili, W. Liu, T. G. Allen, L. Xu, E. V. Kerschaver, M. Morales-Masis, U. Schwingenschlögl, and S. D. Wolf, *Zr-Doped Indium Oxide (IZRO) Transparent Electrodes for Perovskite-Based Tandem Solar Cells,* Advanced Functional Materials **29**, 1901741 (2019).

[74] M. Zhang, Q. Chen, R. Xue, Y. Zhan, C. Wang, J. Lai, J. Yang, H. Lin, J. Yao, Y. Li, L. Chen, and Y. Li, *Reconfiguration of interfacial energy band structure for high-performance inverted structure perovskite solar cells,* Nature Communications 2019 10:1 **10**, 1 (2019).

[75] R. Pandey and R. Chaujar, *Technology computer aided design of 29.5% efficient perovskite/interdigitated back contact silicon heterojunction mechanically stacked tandem solar cell for energy-efficient applications,* J. of Photonics of Energy **7**, 022503 (2017).

[76] W. Rehman, D. P. McMeekin, J. B. Patel, R. L. Milot, M. B. Johnston, H. J. Snaith, and L. M. Herz, *Photovoltaic mixed-cation lead mixed-halide perovskites: links between crystallinity, photostability and electronic properties,* Energy & Environmental Science **10**, 361 (2017).

[77] Y. Kim, E. H. Jung, G. Kim, D. Kim, B. J. Kim, and J. Seo, *Sequentially Fluorinated PTAA Polymers for Enhancing VOC of High-Performance Perovskite Solar Cells,* Advanced Energy Materials **8**, 1801668 (2018).

[78] R. Kotipalli, O. Poncelet, G. Li, Y. Zeng, L. A. Francis, B. Vermang, and D. Flandre, *Addressing the impact of rear surface passivation mechanisms on ultra-thin Cu(In,Ga)Se2 solar cell performances using SCAPS 1-D model,* Solar Energy **157**, 603 (2017).

[79] T. M. Friedlmeier, P. Jackson, A. Bauer, D. Hariskos, O. Kiowski, R. Wuerz, and M. Powalla, *Improved Photocurrent in Cu(In,Ga)Se2 Solar Cells: From 20.8% to 21.7% Efficiency with CdS Buffer and 21.0% Cd-Free,* IEEE Journal of Photovoltaics **5**, 1487 (2015).

[80] T. Hara, T. Maekawa, S. Minoura, Y. Sago, S. Niki, and H. Fujiwara, *Quantitative assessment of optical gain and loss in submicron-textured CuIn1-xGaxSe2 solar cells fabricated by three-stage coevaporation,* Physical Review Applied **2** (2014), 10.1103/PhysRevApplied.2.034012.

[81] H. Tang, Y. Shang, W. Zhou, Z. Peng, and Z. Ning, *Energy Level Tuning of PEDOT:PSS for High Performance Tin-Lead Mixed Perovskite Solar Cells,* Solar RRL **3**, 1 (2019).

[82] A. J. Olivares, I. Cosme, M. E. Sanchez-Vergara, S. Mansurova, J. C. Carrillo, H. E. Martinez, and A. Itzmoyotl, *Nanostructural Modification of PEDOT:PSS for High Charge Carrier Collection in Hybrid Frontal Interface of Solar Cells,* Polymers 2019, Vol. 11, Page 1034 **11**, 1034 (2019).

[83] R. Bernal-Correa and A. Morales-Acevedo, *Spectral reflectance optimization for planar perovskite solar cells,* Optik **227** (2021), 10.1016/j.ijleo.2020.165973.

[84] K. Orgassa, H. W. Schock, and J. H. Werner, *Alternative back contact materials for thin film Cu(In,Ga)Se2 solar cells,* Thin Solid Films **431-432**, 387 (2003).

[85] D. L. Wang, H. J. Cui, G. J. Hou, Z. G. Zhu, Q. B. Yan, and G. Su, *Highly efficient light management for perovskite solar cells,* Scientific Reports 2016 6:1 **6**, 1 (2016).

[86] Z. C. Holman, A. Descoeudres, L. Barraud, F. Z. Fernandez, J. P. Seif, S. De Wolf, and C. Ballif, *Current losses at the front of silicon heterojunction solar cells,* IEEE Journal of Photovoltaics **2**, 7 (2012).

[87] I. P. Romanova, A. V. Bogdanov, I. A. Izdelieva, V. A. Trukhanov, G. R. Shaikhutdinova, D. G. Yakhvarov, S. K. Latypov, V. F. Mironov, V. A. Dyakov, I. V. Golovnin, D. Y. Paraschuk, and O. G. Sinyashin, *Novel indolin-2-one-substituted methanofullerenes bearing long N-alkyl chains: Synthesis and application in bulk-heterojunction solar cells,* Beilstein Journal of Organic Chemistry **10**, 1121 (2014).

[88] H. Wang, B. Cai, and X. Yuan, *Significant light absorption improvement in perovskite/CIGS tandem solar cells with dielectric nanocone structures,* Journal of Physics: Conference Series **844** (2017), 10.1088/1742-6596/844/1/012004.

[89] *Carrier trapping and recombination: the role of defect physics in enhancing the open circuit voltage of metal halide perovskite solar cells,* Energy & Environmental Science **9**, 3472 (2016).

[90] W. E. Sha, H. Zhang, Z. S. Wang, H. L. Zhu, X. Ren, F. Lin, A. K. Jen, and W. C. Choy, *Quantifying Efficiency Loss of Perovskite Solar Cells by a Modified Detailed Balance Model,* Advanced Energy Materials **8**, 1701586 (2018).

[91] J. Wang, W. Fu, S. Jariwala, I. Sinha, A. K. Jen, and D. S. Ginger, *Reducing Surface Recombination Velocities at the Electrical Contacts Will Improve Perovskite Photovoltaics,* ACS Energy Letters **4**, 222 (2019).

[92] J. Idígoras, L. Contreras-Bernal, J. M. Cave, N. E. Courtier, Á. Barranco, A. Borras, J. R. Sánchez-Valencia, J. A. Anta, and A. B. Walker, *The Role of Surface Recombination on the Performance of Perovskite Solar Cells: Effect of Morphology and Crystalline Phase of TiO2 Contact,* Advanced Materials Interfaces **5** (2018), 10.1002/ADMI.201801076.

[93] D. Głowienka, D. Zhang, F. Di Giacomo, M. Najafi, S. Veenstra, J. Szmytkowski, and Y. Galagan, *Role of surface recombination in perovskite solar cells at the interface of HTL/CH3NH3PbI3,* Nano Energy **67**, 104186 (2020).

[94] C. Zhang, H. Wang, H. Li, Q. Zhuang, C. Gong, X. Hu, W. Cai, S. Zhao, J. Chen, and Z. Zang, *Simultaneous passivation of bulk and interface defects through synergistic effect of anion and cation toward efficient and stable planar perovskite solar cells,* Journal of Energy Chemistry (2021), 10.1016/J.JECHEM.2021.07.011.

[95] S. Siebentritt, *What limits the efficiency of chalcopyrite solar cells?* Solar Energy Materials and Solar Cells **95**, 1471 (2011).

[96] D. Koushik, M. Jošt, A. Dučinskas, C. Burgess, V. Zardetto, C. Weijtens, M. A. Verheijen, W. M. M. Kessels, S. Albrecht, and M. Creatore, *Plasma-assisted atomic layer deposition of nickel oxide as hole transport layer for hybrid perovskite solar cells,* Journal of Materials Chemistry C **7**, 12532 (2019).

[97] M. T. Greiner, M. G. Helander, Z.-B. Wang, W.-M. Tang, and Z.-H. Lu, *Effects of Processing Conditions on the Work Function and Energy-Level Alignment of NiO Thin Films,* Journal of Physical Chemistry C **114**, 19777 (2010).

[98] K. V. Rao and A. Smakula, *Dielectric Properties of Cobalt Oxide, Nickel Oxide, and Their Mixed Crystals,* Journal of Applied Physics **36**, 2031 (2004).

[99] M. Köhler, M. Pomaska, P. Procel, R. Santbergen, A. Zamchiy, B. Macco, A. Lambertz, W. Duan, P. Cao, B. Klingebiel, S. Li, A. Eberst, M. Luysberg, K. Qiu, O. Isabella, F. Finger, T. Kirchartz, U. Rau, and K. Ding, *A silicon carbide-based highly transparent passivating contact for crystalline silicon solar cells approaching efficiencies of 24%,* Nature Energy **6**, 529 (2021).

[100] Q. Meng, Y. Chen, Y. Y. Xiao, J. Sun, X. Zhang, C. B. Han, H. Gao, Y. Zhang, and H. Yan, *Effect of temperature on the performance of perovskite solar cells,* Journal of Materials Science: Materials in Electronics **32**, 12784 (2021).

[101] J. Xie, X. Yu, J. Huang, X. Sun, Y. Zhang, Z. Yang, M. Lei, L. Xu, Z. Tang, C. Cui, P. Wang, and D. Yang, *Self-Organized Fullerene Interfacial Layer for Efficient and Low-Temperature Processed Planar Perovskite Solar Cells with High UV-Light Stability,* Advanced Science **4** (2017), 10.1002/advs.201700018.

[102] H. Zhang, F. Ye, W. Li, J. Yao, R. S. Gurney, D. Liu, C. Xiong, and T. Wang, *Bright perovskite light-emitting diodes with improved film morphology and reduced trap density via surface passivation using quaternary ammonium salts,* Organic Electronics **67**, 187 (2019).

[103] W. Shen, Y. Dong, F. Huang, Y.-B. Cheng, and J. Zhong, *Interface passivation engineering for hybrid perovskite solar cells,* Materials Reports: Energy , 100060 (2021).